

The Properties of the Hot Gas in Galaxy Groups and Clusters from 1-D Hydrodynamical Simulations – I. Cosmological Infall Models

P.A. Knight and T.J. Ponman¹

School of Physics and Space Research, University of Birmingham, Edgbaston, Birmingham B15 2TT, UK

ABSTRACT

We report the results of 1-D hydrodynamical modelling of the evolution of gas in galaxy clusters. We have incorporated many of the effects missing from earlier 1-D treatments: improved modelling of the dark matter and galaxy distributions, cosmologically realistic evolution of the cluster potential, and the effects of a multiphase cooling flow. The model utilises a fairly standard 1-D Lagrangian hydrodynamical code to calculate the evolution of the intracluster gas. This is coupled to a theoretical model for the growth of dark matter density perturbations. The main advantages of this treatment over 3-D codes are (1) improved spatial resolution within the cooling flow region, (2) much faster execution time, allowing a fuller exploration of parameter space, and (3) the inclusion of additional physics.

In the present paper, we explore the development of infall models – in which gas relaxes into a deepening potential well – covering a wide range of cluster mass scales. We find that such simple models reproduce many of the global properties of observed clusters. Very strong cooling flows develop in these 1-D cluster models. In practice, disruption by major mergers probably reduces the cooling rate in most clusters. The models overpredict the gas fraction in low mass systems, indicating the need for additional physical processes, such as preheating or galaxy winds, which become important on small mass scales.

1 INTRODUCTION

Rich clusters of galaxies have long been known to be strong sources of diffuse X-ray emission, caused by thermal bremsstrahlung from a hot ($T \sim 10^8$ K) intracluster plasma (the intracluster medium, or ICM). This gas is the dominant baryonic component in such systems, contributing 20–30% of the gravitating material within an Abell radius. More recently, it has become clear that such a diffuse component is also present in poor clusters and galaxy groups. A good understanding of the processes involved in the formation and evolution of this diffuse gas is therefore of key importance for any complete theory of structure formation over a large range of scales.

The earliest numerical models of the evolution of the intracluster gas (Gull & Northover 1975; Lea 1976; Takahara *et al.* 1976) were all one-dimensional simulations, concerned primarily with the evolution of uniform density gas ‘clouds’ relaxing into static potentials formed by the cluster galaxies and dark matter. In this simple situation, infall of gas leads to a rise in central gas density, and a shock propagates outwards from the centre of the cluster, heating the gas to temperatures similar to those observed today. After passage of the shock, the gas is approximately in hydrostatic equilibrium and further evolution is quasistatic. The subsequent cluster luminosity is found to be

¹To whom correspondence should be addressed.

nearly constant, although Lea (1976) found large fluctuations in L_X , probably due to numerical problems. The resulting gas distributions are generally not well fitted by any polytropic distribution, although Gull & Northover (1975), who considered large radius infall into an initially empty potential, found that the cluster gas distributions were almost adiabatic.

Perrenod (1978) considered more realistic infall models in which the cluster potential varies with time, using the results of an N -body simulation of the evolution of the galaxies in a Coma-like cluster (White 1976). In these simulations, the cluster galaxies collapse rapidly by violent relaxation, followed by a slower contraction due to two-body encounters. Unlike models with a static potential, the cluster X-ray luminosity was found to rise by an order of magnitude from $z = 1$ to $z = 0$ (for a flat Einstein-de Sitter cosmology), due primarily to the deepening of the potential well. However, this rate of evolution is considerably larger than that observed and may reflect overmerging in the galaxy distribution – White’s models assumed that all the cluster mass was bound to the galaxies, overestimating the strength of two-body encounters.

Hirayama (1978) extended the purely primordial simulations and considered models including mass and energy injection from a static galaxy distribution. These simulations showed that the injected material dominated the ICM towards the centre, primarily because the gas distribution in the cluster was more extended than that assumed for the galaxies. For high gas injection temperatures ($T_{inj} \gtrsim 3 \times 10^8$ K) a cluster wind formed.

More recently, much effort has been expended on the development of 3-D codes that are able to calculate the evolution of the gas and one or more collisionless components (e.g. dark matter, galaxies) from the primordial density fluctuation spectrum. This allows a fully self-consistent treatment in which the ICM evolves in a three-dimensional, time-varying potential. Since hierarchical clustering models will, for many interesting power spectra, lead to a high degree of substructure at all stages of the evolution, grid-based hydrodynamical techniques with their limited spatial resolution are unable to evolve the different levels of clustering hierarchy simultaneously. The gas flow is therefore generally calculated using particle-based techniques, for example smoothed particle hydrodynamics (SPH; Gingold & Monaghan 1977), coupled with a suitable N -body algorithm (e.g., P³M; Efsthathiou & Eastwood, 1981).

Several authors have computed 3-D evolutionary models using such techniques – e.g., Evrard (1988, 1990), Thomas & Couchman (1992), Katz & White (1993), Metzler & Evrard (1994), Navarro, Frenk & White (1996), hereafter NFW96. In most cases, cluster cores are found to develop at the intersection of filaments and sheets, and cluster growth proceeds through accretion of surrounding material as well as through mergers with smaller, collapsed systems.

Although the general problem of non-linear evolution requires resort to numerical techniques, it is possible to study the evolution of structure in hierarchical models of the Universe by exploiting the approximate self-similarity of the evolution expected under certain conditions: namely those in which the background universe has closure density ($\Omega = 1$), so the Universe is scale free, and in which the amplitude of the initial density fluctuations follows a power-law, so these perturbations are also scale free. In this situation, the clustering is self-similar in the sense that statistical properties of the cluster population must evolve according to simple scaling laws (Kaiser 1986).

In the idealised case of the spherically symmetric growth of an overdense region within an environment in which the overdensity varies initially as a power law function of radius, the evolution of *individual* clusters develops in a self-similar fashion (Fillmore & Goldreich 1984 (FG84); Bertschinger 1985). In this case, the profiles of a growing cluster at different epochs are similar, and clusters of different mass at a given epoch are simply scaled versions of one another. Since it has been shown by Hoffman & Shaham (1985) that the mean primordial overdensity distribution about a local peak does take a power law form, one might expect such self-similar growth to give a reasonable approximation to the mean growth of a cluster.

In practice, the similarity will be disturbed by departures from spherical symmetry, and by

interaction between neighbouring density peaks. Nonetheless, simulations (e.g. Navarro, Frenk & White 1995, NFW96) indicate that when additional physics, such as radiative cooling and injection of winds from galaxies, is not included, cluster growth *is* approximately self-similar, with density profiles similar in form to those predicted by infall models of cluster formation (FG84; Bertschinger 1985). Also, clusters of different mass are very similar when appropriately scaled – though when a wide mass range is considered, lower mass systems are found to be rather more centrally concentrated, since they tend to form earlier. These results encourage the idea that 1-dimensional simulations should give a reasonable approximation to the mean evolution of clusters.

Since previous 1-D treatments were too simplistic (none combined a realistic evolving potential with gas injection and cooling), and the limits of present day computers mean that 3-D simulations have poor resolution ($\gtrsim 100$ kpc), numerical simulations have thus far been unable to shed much light on a number of unanswered questions: e.g., Do the scaling laws break down when cooling is included? Were cooling flows more massive in the past? How does the mass deposition rate vary with radius and system size? How does the gas mass fraction vary with radius? How does the cluster luminosity vary with time?

The purpose of the present study is to address some of these questions, using a 1-D code, *EVOL*, that incorporates many of the effects missing from the older 1-D treatments: improved modelling of the dark matter and galaxy distributions, more realistic gas injection mechanisms, the effects of convection and multiphase cooling, as well as a simple investigation of the effects of mergers.

The model utilises a fairly standard 1-D Lagrangian hydrodynamical code to calculate the evolution of the intracluster gas. This code is coupled to a theoretical model for the growth of dark matter density perturbations, which gives a cluster potential that deepens in a cosmologically realistic way with time. The main advantages of this treatment over 3-D codes are (1) improved spatial resolution within the cooling flow region, (2) fast execution time, allowing a fuller exploration of parameter space, and (3) the inclusion of additional physics. The main disadvantage is that we are unable to accurately model the effects of asymmetric processes, such as cluster mergers. This limitation, however, does not invalidate our results since, although the evolution of the dark matter in clusters is complex, with many clusters showing evidence of substructure, the dark matter distribution in “quiescent” clusters can be reasonably well approximated by a spherically symmetric model. For example, recent simulations by Tormen, Bouchet & White (1996) show that dark matter halos spend about two thirds of their evolution in a relaxed state, during which the density profiles of the halos are well approximated by the NFW96 analytical model. Having said this, periodic major mergers may well have a substantial impact on the structure within the central cooling flow region, possibly disrupting the flow. We investigate this effect below, using a simple model for the change in entropy of the gas within the cooling flow following a merger.

Our aim is to determine the role of, and place constraints on, the heating and cooling processes that are important for the evolution of the ICM. The current paper deals with models in which the intracluster gas is unaffected by injection of energy and heavy elements from cluster galaxies, in order to test the extent to which the observed properties of clusters and groups can be explained by models with gas dynamics and radiative cooling, without recourse to additional physics. Models with gas injection from the galaxies are considered in a second paper (Paper II – Ponman and Knight, in preparation).

The layout of the paper is as follows: the equations on which the code is based, and the numerical methods employed, are outlined in Section 2, and some test runs used to verify the accuracy of the code are described in Section 3. A large number of simulations have been run, in order to investigate the mass dependence of the evolution, and to check the effect of varying a number of key physical parameters. This grid of models is described in Section 4, and the evolution of the hot gas which results is discussed in broad terms in Section 5. Some more detailed aspects

of the properties of these simulated clusters are then investigated: cooling flows in Section 6, the distribution of hot gas in Section 7, and the evolution of the X-ray luminosity in Section 8. The simulations presented here assume an $\Omega = 1$ Universe, however in Section 9 we examine briefly the impact of a lower value of Ω on the X-ray evolution, and conclude that it is not large. Finally, in Section 10, we summarise our conclusions.

2 NUMERICAL METHOD

2.1 Basic Equations

Assuming spherical geometry, the evolution of the ICM in galaxy clusters is described by the standard time-dependent equations of gas dynamics (Mathews & Baker 1971), with additional terms to remove gas from the flow when the cooling time is sufficiently short in order to simulate the features of an inhomogeneous cooling flow. Under such conditions, the equations of mass, momentum, and energy conservation that govern the evolution of the ICM are

$$\frac{\partial \rho}{\partial t} + \frac{1}{r^2} \frac{\partial(r^2 \rho u)}{\partial r} = -\omega \rho, \quad (1)$$

$$\frac{Du}{Dt} = -\frac{1}{\rho} \frac{\partial(p+q)}{\partial r} + g, \quad (2)$$

$$\frac{D\epsilon}{Dt} - \frac{p+q}{\rho^2} \frac{D\rho}{Dt} = -\frac{n_e n_H}{\rho} \Lambda, \quad (3)$$

where D/Dt is the Lagrangian derivative, u the radial gas velocity (positive for outflow), ρ the ICM mass density, n_e the electron number density, n_H the hydrogen number density, and ω accounts for gas lost by cooling (see section 2.2 below). For a gas with ratio of specific heats $\gamma = 5/3$, the specific energy ϵ and the gas pressure p are equal to $3kT/(2\mu m_p)$ and $\rho kT/(\mu m_p)$ respectively, where T is the gas temperature, k is the Boltzmann constant and m_p is the proton mass. Throughout this paper we take $\mu = 0.6$ and $\mu_e = 1.15$, appropriate for a fully-ionized plasma composed of 90% hydrogen and 10% helium by number.

The term q in Equations 2 and 3 is the artificial viscosity (Richtmyer & Morton 1967),

$$q = \rho \left(a \min \left\{ \frac{\partial u}{\partial r}, 0 \right\} \right)^2, \quad (4)$$

which is effective at smoothing the boundaries of shock waves. The parameter a determines the thickness of the shock front. Setting $a = 2$, the value that is adopted throughout this paper, ensures accurate modelling of the shock by spreading the jump in parameter values over several Lagrangian shells.

2.2 Radiative Cooling and Mass Deposition

The term on the right hand side of the energy equation accounts for the effect of radiative cooling. Λ is evaluated using bilinear interpolation from tabulated versions of the cooling function of Raymond, Cox, & Smith (1976) for primordial and solar abundances,

$$\Lambda\{T, Z\} = (1 - Z)\Lambda\{T, 0\} + Z\Lambda\{T, 1\}, \quad (5)$$

where Z is the metallicity of the gas. Compton cooling is only important at high redshift ($z \gtrsim 10$), and is ignored in the simulations presented here. At such early epochs additional energy input from early star formation is likely to be effective at preheating the cluster gas. The effects of this will be explored in Paper II.

Observed X-ray surface brightness profiles in cooling flows imply that gas cools and is deposited throughout the flow (Fabian, Nulsen & Canizares 1991). The treatment of mass deposition used in *EVOL* is similar to that of David, Forman & Jones (1990). Gas is assumed to be thermally unstable to entropy perturbations when $(2 - d \ln \Lambda / d \ln T) > 0$ (David, Forman & Jones 1990). When this condition is satisfied, and the integrated isobaric cooling time, t_{cool} is less than $\alpha_{md} t$, gas is removed from the ICM at the rate $\xi \rho / t_{rad}$, where ρ is the gas density, t_{rad} is the local instantaneous cooling time, and α_{md} and ξ are model parameters. Theoretical considerations and observations of the cooling flows in rich clusters suggest $\xi \sim 1$ (Sarazin 1990). This accounts for the last term in Equation 1,

$$\omega = \begin{cases} \xi / t_{rad}, & \text{if } (2 - d \ln \Lambda / d \ln T) > 0 \text{ and } t_{cool} < \alpha_{md} t \\ 0, & \text{otherwise} \end{cases} \quad (6)$$

2.3 The Cluster Potential

The gravitational acceleration (g in Equation 2) is given by,

$$g = -\frac{G}{r^2} [M_{dark}(r) + M_{ICM}(r) + M_{dep}(r)], \quad (7)$$

where $M_{dark}(r)$, $M_{ICM}(r)$ and $M_{dep}(r)$ are the total dark matter, ICM and ‘cooled’ gas mass within radius r respectively. The cooled gas mass, M_{dep} , is primarily used for book-keeping, keeping track of material that is lost from the ICM due to mass deposition, although in the simulations it was found to be dynamically important close to the cluster centre at later times. The dark matter distribution otherwise dominates the dynamical evolution of the ICM. The galaxy distribution is only important in models with significant feedback from galaxy winds and ram-pressure stripping and is not considered here. (The galaxies are effectively incorporated into the dark matter component.)

The evolution of the dark matter in clusters is complex, with many clusters showing evidence for recent mergers. However, the dark matter distribution in quiescent clusters is reasonably well approximated by a spherically symmetric model. NFW96 found that the radial dark matter density profiles of their simulated clusters were approximately self-similar, with profiles at large radii similar in form to that predicted by analytic infall models (FG84; Bertschinger 1985). In these models, the physical mass distribution of a cluster growing by the 1-D accretion of surrounding material at time t may be calculated by scaling a canonical function to the characteristic size ($R_{vir}(t)$) of the system. We assume that such models give a good approximation to the shape and evolution of the dark matter distribution of real clusters, and adopt the canonical profile given by the similarity solution of FG84 corresponding to $n = -1$ (see Hoffman & Shaham 1985), which matches the slope of the CDM power spectrum on cluster scales (Kaiser 1986). This model tends towards the critical background density ρ_c at large radii. Cusps in the density arising from the turnaround of particle shells are present in the similarity solution. In practice, such features would be washed out by departures from perfect spherical symmetry – we therefore eliminate them by fitting a power law profile to the formal similarity solution.

Following the $n = -1$ similarity solution, the full dark matter profile at $z = 0$ is determined by a single parameter, which may be taken to be the total mass inside the virial radius R_{vir} (defined throughout this work as the radius within which the mean density of the system is $200\rho_c$). The profile at any earlier epoch is then simply a self-similar scaling of this; ρ/ρ_c being a constant function of r/R_{vir} .

There is evidence from N-body simulations that the self-similar model breaks down at small radii, where some flattening of the density distribution is observed. Following the results of NFW96, we therefore flatten the canonical density profile to a logarithmic slope of -1 within a radius

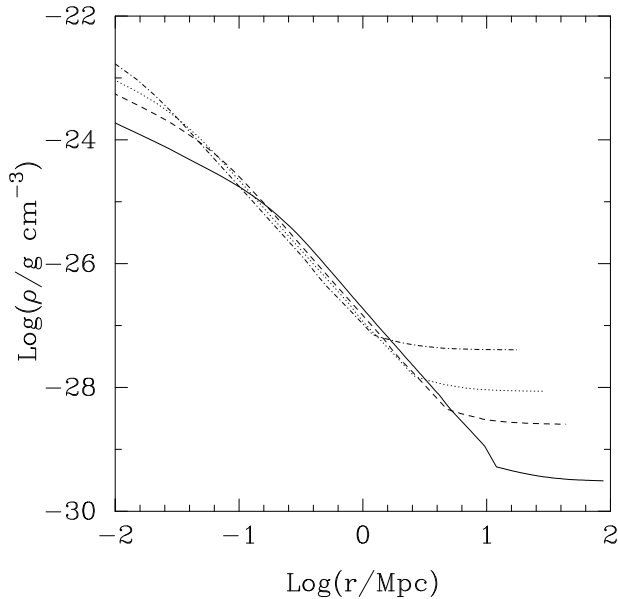


Figure 1: Evolution of the dark matter density in a model with $M_{vir} = 1.6 \times 10^{15} M_{\odot}$. The profile evolves in a self-similar way through redshifts 4 (dot-dash), 2 (dotted), 1 (dashed) and 0 (solid).

of $\eta_{\rho} R_{vir}$, where η_{ρ} is a selectable model parameter. The gas is allowed to evolve within this developing dark matter distribution, and the total gravitational potential is computed from the combined contributions of dark matter, free gas, and gas deposited by cooling.

The evolution of the dark matter distribution in physical units, for the case of a cluster with virial mass $M_{vir} = 1.6 \times 10^{15} M_{\odot}$ at $z = 0$, is shown in Figure 1. In scaled units, ρ/ρ_c versus r/R_{vir} , these curves would all fall on top of one another.

Our approach contrasts with 1-D methods which are based on numerical integration of the equations of motion governing the evolution of collisionless dark matter shells (Thoul & Weinberg 1995). While such methods are more self-consistent than our approach (in the sense that the effect of the gas distribution can be included in the calculation of the dark matter dynamics) there is a high price to pay in terms of the execution speed of the code, since a large number of dark matter shells is required to avoid spurious shocks arising in the gas due to fluctuations in the mass distribution. Our approach has the advantage of avoiding this computational overhead whilst yielding a good approximation to the expected evolution – at large radii the evolution calculated by numerical integration will be similar to that given by the analytic solution since the gas and dark matter are distributed similarly. Only at relatively small radii, where the gas and dark matter distributions can be significantly different, are the two methods likely to differ, but it is precisely at this point that 3-D simulations suggest that 1-D treatments break down, presumably due to the effect of merging, and the dark matter density profile flattens. We are able to incorporate this effect into our model heuristically, by imposing a core on our dark matter distribution.

Equations 1–3 are solved using a standard, first-order, explicit finite-difference Lagrangian scheme (Richtmyer & Morton 1967), with additional terms to account for gravity, cooling, and mass deposition. A useful description of the use of a Lagrangian code in relation to cluster cooling flows is given by Thomas (1988). Full details of our method are given in Knight (1996).

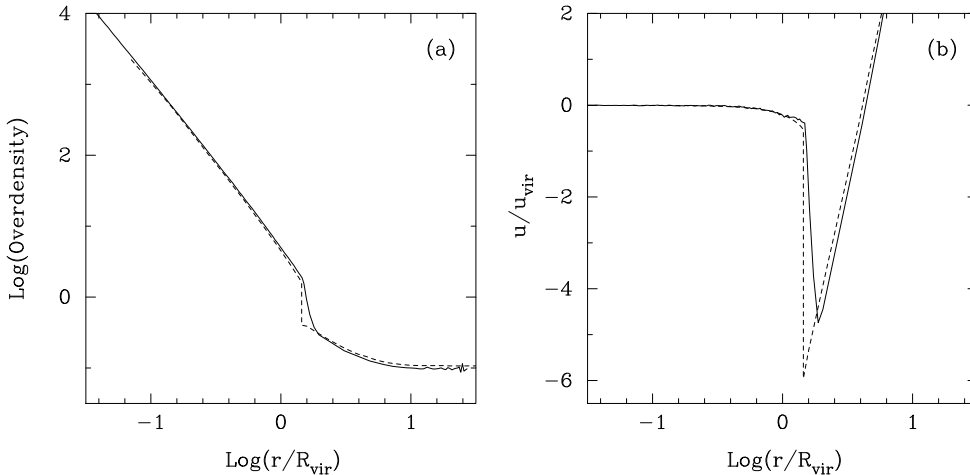


Figure 2: Gas density and velocity profiles from *EVOL* (solid lines) compared with those predicted by self-similar theory (dashed lines; Bertschinger 1985). R_{vir} is the virial radius and $u_{vir} \equiv R_{vir}/t$. The gas (baryon) fraction was taken to be 0.1.

3 TESTS OF THE CODE

The code was subjected to a variety of tests, including comparison with analytically soluble problems, previous hydrodynamical simulations, and with the results of another 1-D Lagrangian code, kindly supplied by Peter Thomas. Full details of these checks are given in Knight (1996). Here we show the results of two of the most important tests – comparisons with the analytical evolution derived for a simple 1-D problem by Bertschinger, and with the results of 3-D simulations which incorporate the effects of hierarchical merging.

3.1 Bertschinger Infall Model

One of the most powerful tests for a hydrodynamical code is the simulation of a self-similar system whose behaviour is known analytically. Such a comparison is useful since any departures of the simulation from the self-similar behaviour will be attributable to a combination of numerical effects and possibly to differences between the model and the simulated system (e.g., different boundary conditions).

Since the evolution of the dark matter profile is given by the infall solution of FG84, in the absence of cooling and injection terms the evolution of the gas in the case of a point perturbation ($n = 0$) will follow that derived by Bertschinger (1985). Figure 2 shows the scaled gas density and velocity profiles for an *EVOL* model with $n = 0$ compared with that predicted analytically. Clearly, there is excellent agreement between the profiles. The only significant differences occur in the shock region, which is spread out over several shells in the *EVOL* solutions.

3.2 Comparison with a 3-D Code

We have also performed some tests to investigate the differences between *EVOL* calculations and those of a 3-D hydro code (Katz & White 1993). For these simulations of an $\Omega = 1$ universe with a CDM initial power spectrum (modelled as an $n = -1$ self-similar hierarchy in the case of *EVOL*),

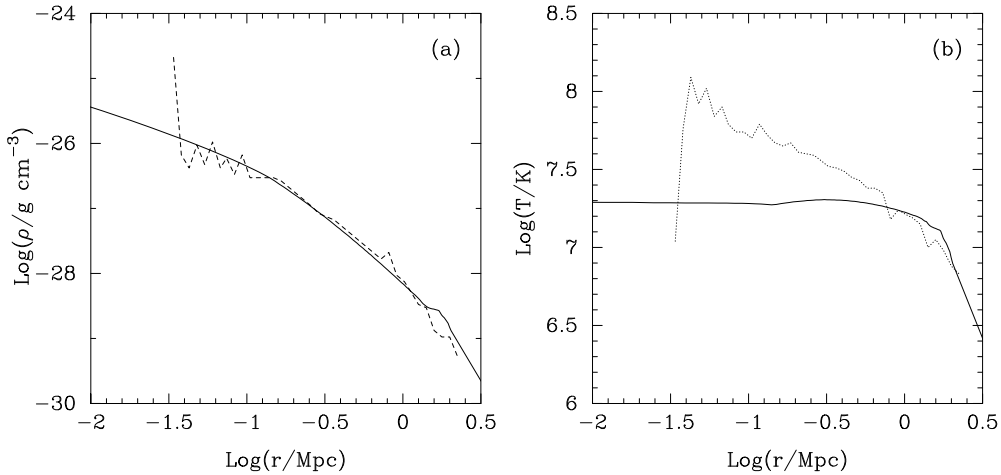


Figure 3: Gas density and temperature profiles calculated by *EVOL* compared with those calculated by a 3-D code (dotted line; Katz & White 1993).

9% of the mass was taken to be in the form of gas, the rest in dark matter. Radiative cooling was included. In the 3-D calculation, a cluster was found to form at the intersection of filaments, forming an object with virial radius $R_{\text{vir}} = 880$ kpc and mass $M_{\text{vir}} = 1.83 \times 10^{14} M_{\odot}$ by $z = 0.13$ when the simulation was halted. The gas density and temperature of this structure is compared to that calculated by *EVOL* in Figure 3 – the initial conditions were taken to be as close to those of the 3-D code as possible, and the normalisation of the initial perturbation was determined from the virial mass of the final object in the 3-D simulation.

There is excellent agreement in the shape of the gas density profile at essentially all radii, apart from the sudden increase in the density at the centre in the 3-D case due to the central ‘cooling catastrophe’ (which is avoided in *EVOL* by the distributed gas deposition). The temperature profiles agree quite well for $r \simeq 1\text{--}3$ Mpc, but that from the 3-D simulation is much more centrally peaked than that from *EVOL*. This is due to the rapid deepening of the potential well as gas near the centre clumps under its own self-gravity, becomes even denser and cools even more rapidly, leading to the formation of a much deeper cluster potential in the 3-D case. However, Katz and White comment that the effect would be reduced if star formation was included (gas can cool and stars cannot, reducing the rate at which the potential well can deepen), which is effectively what is modelled by the multiphase treatment employed by *EVOL*. Such central temperature gradients are typically absent in 3-D treatments in which cooling is neglected (e.g., Evrard 1990; NFW96), most of which yield simulated clusters in which the central regions are essentially isothermal (in general agreement with observation, as discussed in Section 5). Given the high sensitivity of the results from such treatments to details of the model, we consider the agreement between *EVOL* and 3-D codes to be satisfactory.

4 THE MODEL GRID

One of the main advantages of a 1-D treatment is the fast execution time, enabling a much fuller exploration of parameter space than would be possible with a 3-D code. This is very useful since

the possible parameter space for models of the intracluster medium is large, and many of the key parameters that can influence the evolution of the ICM are uncertain. In addition, we are especially interested in the way that the properties of the ICM scale with system size. We have therefore constructed a multidimensional grid that encompasses these parameters, as well as a large range in system size, and calculated the evolution of models at a large number (~ 150) of points in the parameter space.

Each model starts with 200 radial shells at $z = 100$, early enough that the assumed initial gas profiles have negligible effect on the profiles for $z \lesssim 10$. The gas density and velocity were set to $\rho(r) = f_{gas}\rho_{dark}(r)$, and $u(r) = H_i r$ (i.e., comoving with the Hubble flow) respectively, where $\rho_{dark}(r)$ is the initial dark matter density profile (following FG84) and H_i is the Hubble constant at the initial epoch. In practice, if a dark matter concentration has formed, then the initial gas velocity will actually be somewhat perturbed from the Hubble expansion. However, by starting at $z = 100$, we ensure that this has a negligible effect on the evolution. The initial gas temperature was taken to be low ($T(r) = 10^5$ K), ensuring that the initial entropy of the gas is much lower than that typically found in the cores of groups and rich clusters. A large initial entropy for the gas would effectively introduce a scale size into the evolution, leading to the formation of a gas density core. The iron abundance of the gas was set to $Z(r) = 0.4$, consistent with observed mean abundances. In effect, we assume in the present set of models that metals are injected into the ICM at some very early stage in cluster evolution – for example, by Population III stars (e.g. Carr 1994; Ostriker & Gnedin 1996).

The initial dark matter and gas mass fractions for most of the runs were set to $f_{dark} = 0.8$ and $f_{gas} = 0.2$ respectively. This represents a baryon fraction of $f_b \simeq 0.2$, higher than that generally used for cluster simulations ($f_b \simeq 0.1$), and also conflicts (if $\Omega = 1$) with the current restrictive constraints on the universal baryon density parameter from primordial nucleosynthesis calculations, $\Omega_b = 0.05 \pm 0.01 h_{50}^{-2}$ (Walker *et al.* 1991). However, these constraints are also in severe conflict with the observed baryon fractions in clusters of galaxies, 10–20% at 1 Mpc (White & Fabian 1995), rising to $\simeq 30\%$ at the virial radius (David, Jones & Forman 1995). Various possible explanations for this difference have been proposed (White *et al.* 1993), some of which appeal to $\Omega_0 \simeq 0.3$, while others suggest that, within an $\Omega = 1$ framework, baryons were preferentially concentrated within clusters at an early epoch, as a result of an unknown, non-gravitational mechanism. We take the view that, until this issue is resolved, it is preferable to set the baryon fraction in the protoclusters to ≈ 0.2 , rather than produce models in which present day clusters are considerably underdense in baryons compared to observation. However, some low baryon density models with $f_{dark} = 0.9$ and $f_{gas} = 0.1$ have also been investigated in order to bracket the observed baryon fraction range in clusters and groups. In addition, we have constructed some models to explore the effects of a lower density Universe ($\Omega_0 = 0.3$) on the evolution.

By varying the mass enclosed within the virial radius (M_{vir}) at $z = 0$ between $7.8 \times 10^{12} M_\odot$ and $1.6 \times 10^{15} M_\odot$, the grid covers a range of systems from groups with $T_{vir} \lesssim 1$ keV to rich clusters. N-body simulations suggest that the radial infall calculation of the dark matter evolution is unphysical at small radii. NFW96 find that the density profile flattens to a logarithmic slope of approximately -1 near the centre. Our mass profiles were therefore smoothly flattened to $\rho(r) \propto r^{-1}$ within a “core radius” of $0.1 R_{vir}$, in accordance with their result. The results presented here are relatively insensitive to the value of η_ρ , since cooled gas generally becomes the dominant gravitational component at small radii.

The mass deposition parameter was set to $\xi = 1.7$ for shells where $t_{cool} < \alpha_{md} t$, and $\xi = 0$ otherwise. Within the context of the mass deposition model, values of $\xi \sim 1$ have both some theoretical and observational justification: if ξ is too large the gradient of the specific entropy changes sign and the region becomes convectively unstable, effectively reducing ξ back to ~ 1 (Fabian, Nulsen & Canizares 1991). The value $\xi = 1.7$ was chosen since it was found to lead to

Parameter	Name	Units	Values
Density parameter	Ω_0	—	0.3, 1
Gas mass fraction	f_{gas}	—	0.1, 0.2
Final virial mass	M_{vir}	M_\odot	7.8×10^{12} , 2.0×10^{13} , 3.9×10^{13} , 7.8×10^{13} , 2.0×10^{14} , 3.9×10^{14} , 7.8×10^{14} , 1.6×10^{15}
Mass deposition rate	ξ	—	1, 1.7, 2.5
Mass deposition threshold	α_{md}	—	0.2, 1, ∞

Table 1: Summary of the range of model parameters.

the formation of simulated deposition profiles of the form $\dot{M}(r) \propto r$, similar to the form inferred from deprojection analyses of cluster cooling flows (Fabian, Nulsen & Canizares 1991). However, some simulations with $\xi = 1$ and $\xi = 2.5$ have also been performed.

The mass deposition cutoff at $t_{cool} > \alpha_{md}t$ is somewhat arbitrary, although if deposition were to occur with $\xi \sim 1$ out to large radii, the resulting cluster spectra conflict with observations – for example, *Ginga* observations of the Perseus cluster appear to rule out all but a modestly multiphase ICM (Allen *et al.* 1992). $\alpha_{md} = 1$ was used for most of the runs, although the effect of confining mass deposition to the region $t_{cool} < 0.2t$ has also been explored. Mass deposition reduces the mass of shells within the cooling flow region, helping to improve the resolution of the runs – shells are dropped when their mass falls below $10^6 M_\odot$, and any remaining mass is added to a static Eulerian grid which is included in the calculation of the cluster potential.

5 MODEL EVOLUTION

The parameter space for the cluster models has many dimensions. It is therefore convenient to adopt standard values for the model parameters and then test the effect of alternative values. These standard values are taken to be (1) $\Omega_0 = 1$, (2) gas fraction $f_{gas} = 0.2$, (3) mass deposition rate $\xi = 1.7$, and (4) mass deposition threshold $\alpha_{md} = 1$. In the following discussion attention is focussed on parameters that differ from these standard values. Parameters not explicitly mentioned are assumed to have the ‘standard’ value.

The evolution of a standard model of mass $M_{vir} = 1.6 \times 10^{15} M_\odot$ in physical and “scaled” units is shown in Figures 4 and 5 respectively. The scaled plots were obtained by normalising to the characteristic temperature, velocity and entropy: $T_{vir} = \mu m_p G M_{vir} / (2k R_{vir})$, $u_{vir} = R_{vir} / t$, and $S_{vir} = T_{vir} / \rho_{vir}^{\gamma-1}$, where R_{vir} is the radius within which the mean density, ρ_{vir} , is 200 times the background density at time t . The characteristic temperature, T_{vir} , is 8.0×10^7 K, 3.2×10^7 K, 1.1×10^7 K, and 4.4×10^6 K for models of mass $M_{vir} = 1.6 \times 10^{15} M_\odot$, $3.9 \times 10^{14} M_\odot$, $7.8 \times 10^{13} M_\odot$, and $2.0 \times 10^{13} M_\odot$ respectively. T_{vir} is independent of redshift for $n = -1$.

The evolution at large radius is similar to that of the self-similar solution (e.g., Bertschinger 1985). A particle within the overdense region eventually separates from the Hubble expansion, reaching turnaround, $u = 0$, before collapsing back towards the centre. Before reaching $r = 0$, the fluid particle passes through a shock where the velocity changes discontinuously, after which it

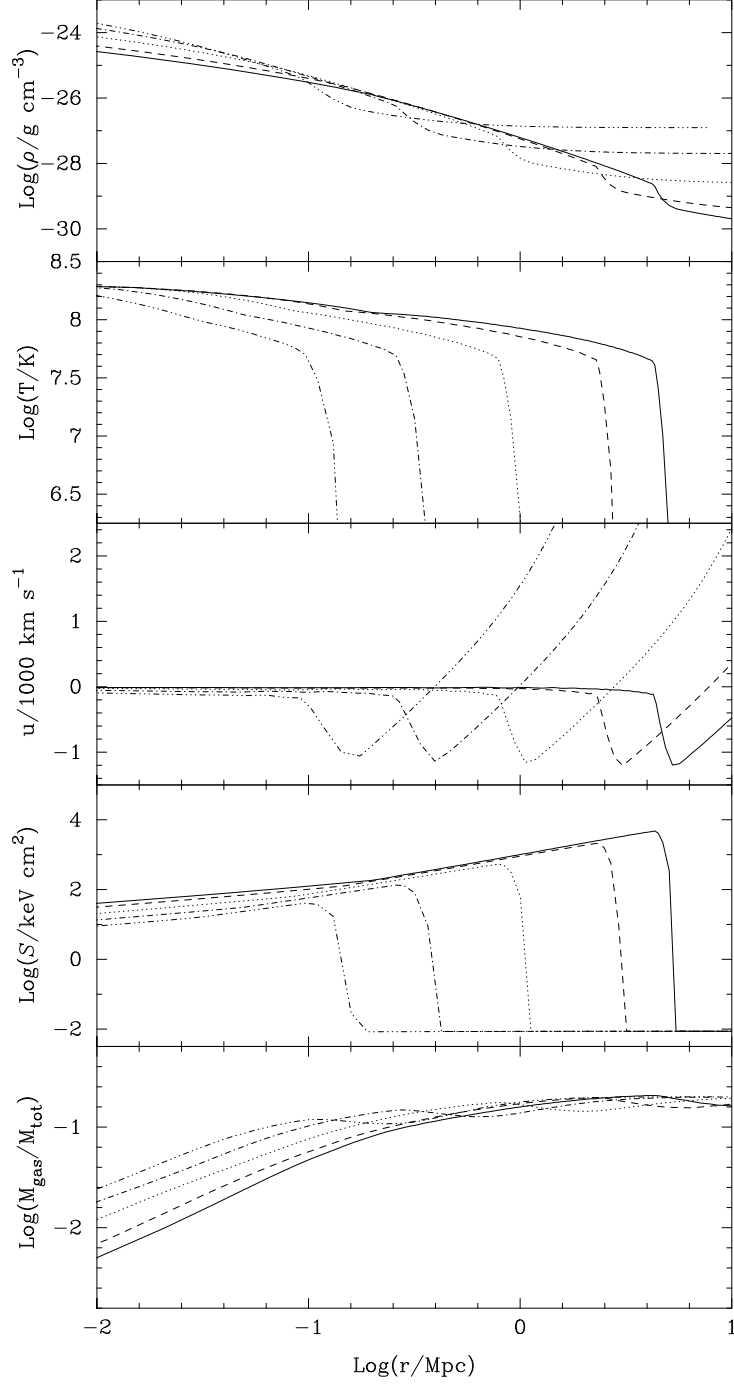


Figure 4: Evolution of the gas density, temperature, velocity, entropy, and enclosed gas mass fraction of a standard model of mass $M_{\text{vir}} = 1.6 \times 10^{15} M_{\odot}$. Redshifts shown are 0, 0.5, 2, 5 and 10 (solid, dashed, dotted, dash-dot-dash, and dash-dot-dot-dot-dash lines respectively).

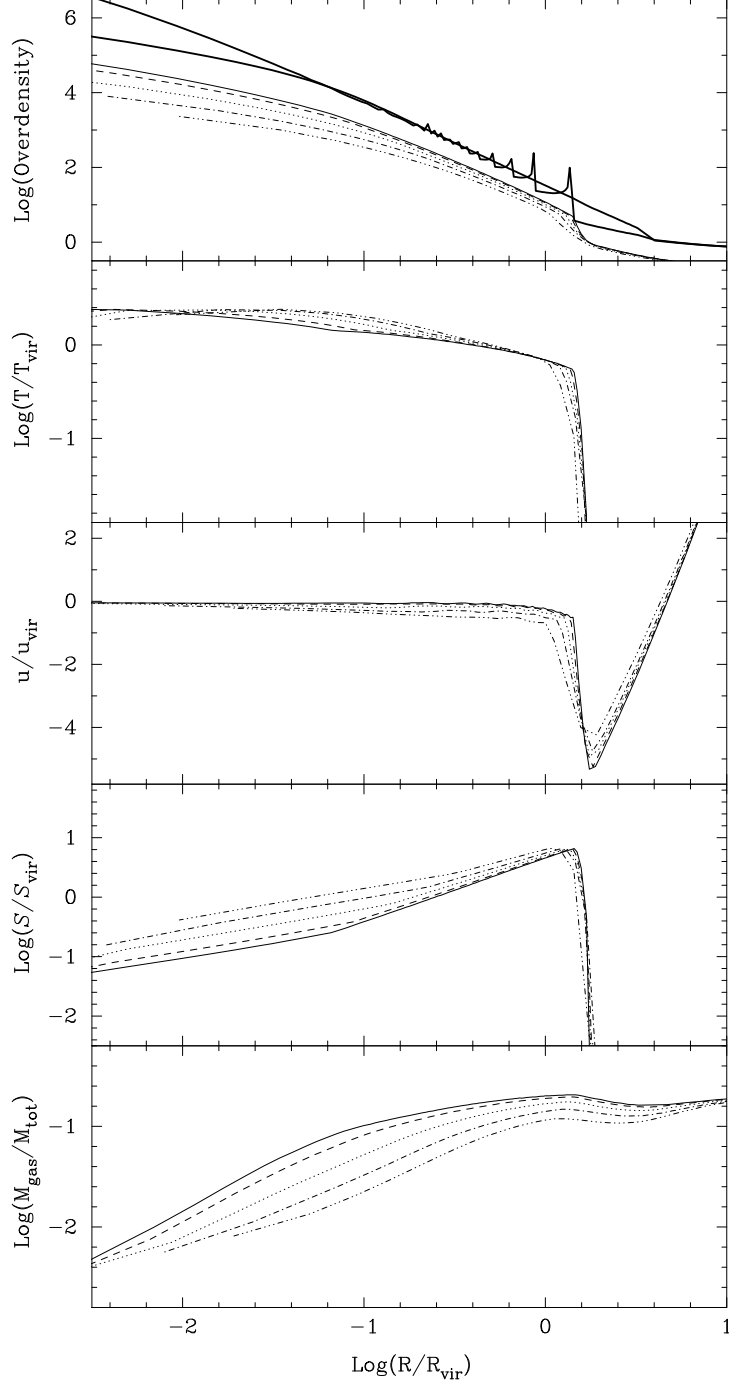


Figure 5: Evolution of the scaled gas density, temperature, velocity, entropy, and enclosed gas mass fraction for a standard model of mass $M_{vir} = 1.6 \times 10^{15} M_{\odot}$. Redshifts shown are 0, 0.5, 2, 5 and 10 (solid, dashed, dotted, dash-dot-dash, and dash-dot-dot-dot-dash lines respectively). The thick solid lines in the top panel show the “unsmoothed” dark matter density profile (with cusps), and the profile represented by a power law with an r^{-1} core applied (see section 2.3).

settles to a constant fraction of its radius at turnaround. In contrast, three dimensional simulations suggest that the kinetic energy of fluid particles is not completely thermalised after passing through the shock. However, the kinetic pressure is only $\sim 10\%$ of the thermal pressure (Evrard 1990) and does not affect the results presented here greatly. The position of the shock is marked by a sharp increase in gas entropy. Within the shock radius, the entropy rises continuously with radius, $S \propto r^{1.3}$, and convection is suppressed.

The density profile, while following the dark matter profile quite well at large radius is strongly affected by cooling and mass deposition nearer the centre. Gas dropped near the cluster centre is replaced by gas of higher entropy from further out, lowering the central gas density. This, coupled with the build-up of a large mass of cooled material produces a strong gradient in the enclosed gas mass fraction. At $z = 0$, the gas mass fraction within 0.5 Mpc, 1 Mpc and 3 Mpc is 0.12, 0.16 and 0.20 respectively. The logarithmic slope of the density profile is found to flatten, from approximately -2 to -1, at a radius of ~ 100 kpc, somewhat less than typically observed core radii in rich clusters, $r_c \simeq 250$ kpc – although many of the systems with the largest core radii may be recent merger remnants. As expected, the effects of cooling are most dramatic at early epochs, when the gas density is higher and the effect of mass deposition consequently more widespread, leading to a reduction in the gas mass fraction throughout the cluster. At later times, cooling is only important near the cluster centre.

Figure 4 shows that the temperature generally declines continuously with increasing radius, even within the cooling flow region. This is not unexpected since the “hot phase” of such a flow is effectively being modelled (the cooling gas is dropped from the ICM at each timestep), and the gas will be adiabatically compressed as it flows inward. Recent studies of multiphase cooling flows within mass profiles with small cores confirm that the temperature of the hot phase will remain approximately constant within the cooling region (Waxman & Miralda-Escudé 1995), while if the gravitating matter distribution is very sharply peaked, as found here, the temperature is expected to rise (White & Sarazin 1987). Beyond this region, the temperature gradient steepens with radius until the sudden drop at the shock. Similar temperature profiles have been found in a number of three dimensional hydrodynamical simulations (e.g. NFW96).

Observations of the temperature structure of clusters have been mostly restricted to the nearest and brightest systems until recently. Observations with coded mask and collimated instruments indicate that the Coma cluster (Hughes, Gorenstein & Fabricant 1988; Watt *et al.* 1992) has an approximately isothermal core within ~ 1 Mpc of the cluster centre with a steep temperature decline at large radius, whilst the Perseus cluster (Eyles *et al.* 1991) shows a modest temperature decline outside the cooling region, with the emission well modelled by a power-law temperature profile, $T(r) \propto r^{-0.30 \pm 0.08}$. Recent results from ROSAT and ASCA (e.g. Allen, Fabian & Kneib 1996; Markevitch & Vikhlinin 1996; Loewenstein & Mushotzky 1996) suggest that most reasonably relaxed clusters have fairly flat temperature distributions within the central ~ 1 Mpc (apart from the common presence of a central cooling flow), although steep gradients at larger radii appear to be present in at least some high temperature clusters (Markevitch 1996).

Figure 6 shows the final ($z = 0$) scaled gas profiles for different mass models. The potentials of these clusters have evolved in a self-similar fashion, as described in section 2.3. If the gas has followed suit, then the profiles in Figure 6 should coincide. At large radius, where there is no additional physics to break the scaling, the scaled profiles are very similar to each other. However, significant differences occur near the cluster centre, where cooling is important.

6 THE COOLING FLOW

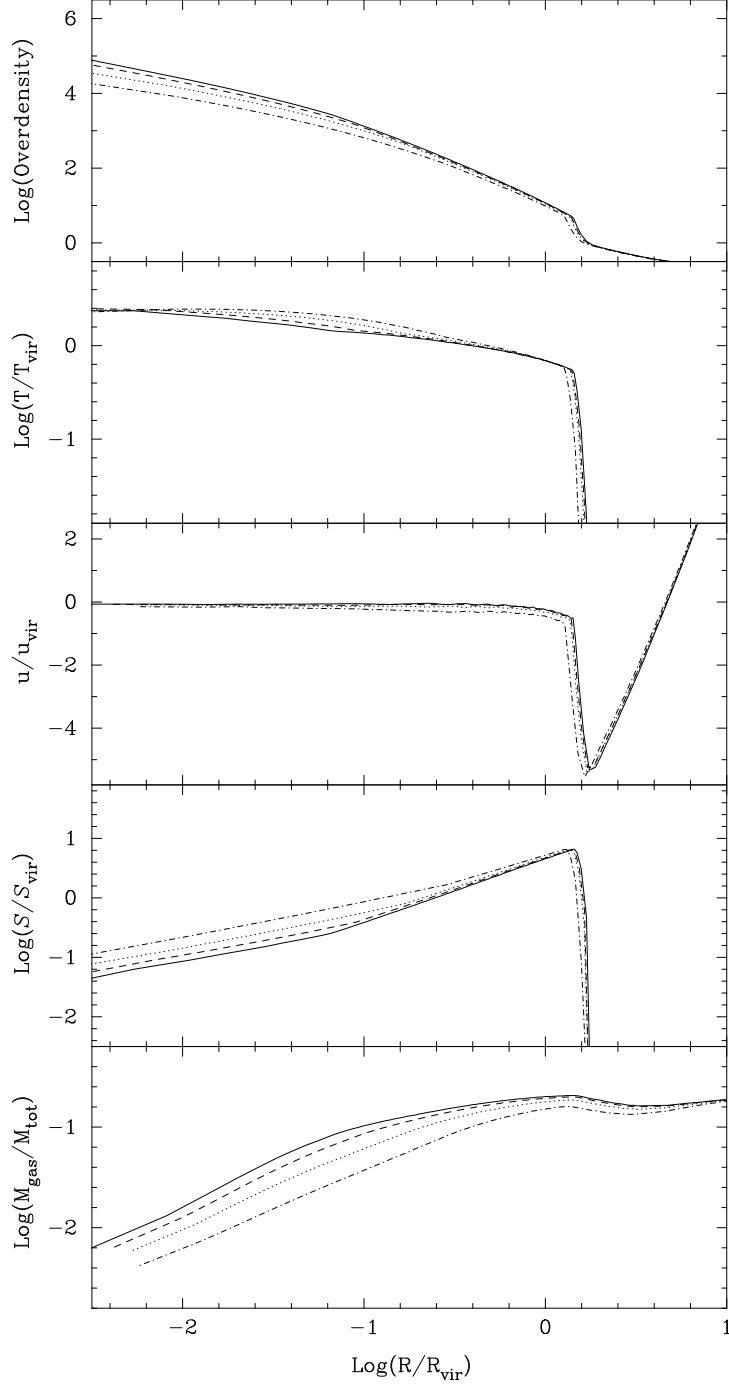


Figure 6: Final scaled gas density, temperature, velocity, entropy, and enclosed gas mass fraction profiles for standard models of mass $M_{\text{vir}} = 2.0 \times 10^{13}$, 7.8×10^{13} , 3.9×10^{14} and $1.6 \times 10^{15} M_{\odot}$ (dot-dash, dotted, dashed, and solid line styles respectively).

6.1 Mass Deposition Profile

As discussed in Section 2.1, the mass deposition parameter ξ was chosen so that the mass deposition profile is similar to observations, $\dot{M}(r) \propto r$ (Fabian, Nulsen & Canizares 1991). The final cumulative mass deposition rate is shown plotted against radius for the $M_{vir} = 1.6 \times 10^{15} M_{\odot}$ model in Figure 7a – within the mass deposition region $\dot{M}(r) \propto r$, as expected. The total mass deposition rate for this model is higher than generally found observationally – $\dot{M} \simeq 2000 M_{\odot} \text{ yr}^{-1}$ compared to typical observed values of $\lesssim 1000 M_{\odot} \text{ yr}^{-1}$, although there are a few exceptional cases with much higher inferred mass deposition rates (e.g. Schindler *et al.* 1996). The density profile of the cooled material is centrally peaked and constitutes the dominant gravitational component at small radii (see Figure 8). The cluster potential is therefore sufficiently peaked that the cooling flow becomes gravity dominated near the cluster centre, and the temperature of the hot phase increases due to adiabatic compression as it flows inwards. As a result of this dominant cooled gas component in the core, the circular velocities near the cluster centre are $v_{circ} \simeq 1500 \text{ km s}^{-1}$ in high mass models – much larger than the velocity dispersions ($\lesssim 400 \text{ km s}^{-1}$, Oegerle & Hoessel 1991) observed in the envelopes of the cD galaxies which are commonly found at the focus of cluster cooling flows. This discrepancy could be reduced by mechanisms not incorporated in the present models, such as cluster mergers distributing the material throughout the core, or preheating of the cluster gas, which reduces the mass of cooled material (see Paper II).

Several possible mechanisms for lowering the mass deposition rate have been explored: lowering the baryon fraction, f_{gas} , artificially reducing the radiative cooling rate, and varying the model parameters governing the deposition of gas in the cooling flow (ξ and α_{md}). The final ($z = 0$) mass deposition profiles for some of these models are shown in Figure 7b-d. Except for the models with low baryon fraction, varying the above parameters has little effect on the total mass deposition rate. To some extent, there is a feedback mechanism which keeps the mass deposition rate at an approximately constant value, regardless of the values specified for the cooling flow parameters – if the cooling rate is reduced for example, the gas simply flows further into the cluster centre (where the density is higher) before dropping out of the flow. The models with reduced baryon fraction have significantly lower mass deposition rates, but the gas mass fraction in these cases is in conflict with observations (White & Fabian 1995), even if the ICM is multiphase (Gunn & Thomas 1995).

Since our attempts at reducing the mass deposition rate by varying the parameters of the code have been unsuccessful, we conclude that the most likely explanations for the discrepancy between the mass deposition rate of the models and values inferred from observations are related to limitations of the model. For example, (1) the spherical geometry assumption, and the neglect of angular momentum that would inhibit gas flowing into the cluster centre, (2) the lack of cluster mergers that would periodically disrupt the cooling flow, and (3) turbulence and thermal conduction within the core. Since both angular momentum and merging would tend to reduce the central density, and hence the mass deposition rate, we believe that our models represent ‘maximal’ cooling flows, giving a useful upper bound to mass deposition rates that might be found observationally. This view receives some support from the observed variation of mass deposition rate with cluster temperature, as discussed in the next section.

The high mass deposition rates of the standard models have a knock-on effect on other quantities, such as the emission-weighted temperature, and X-ray luminosity. Since the lower mass deposition rates of real clusters are likely to be due to physical processes not modelled here, we have shown the effect, in some of the succeeding plots, of arbitrarily reducing these mass deposition rates by a factor of 5.

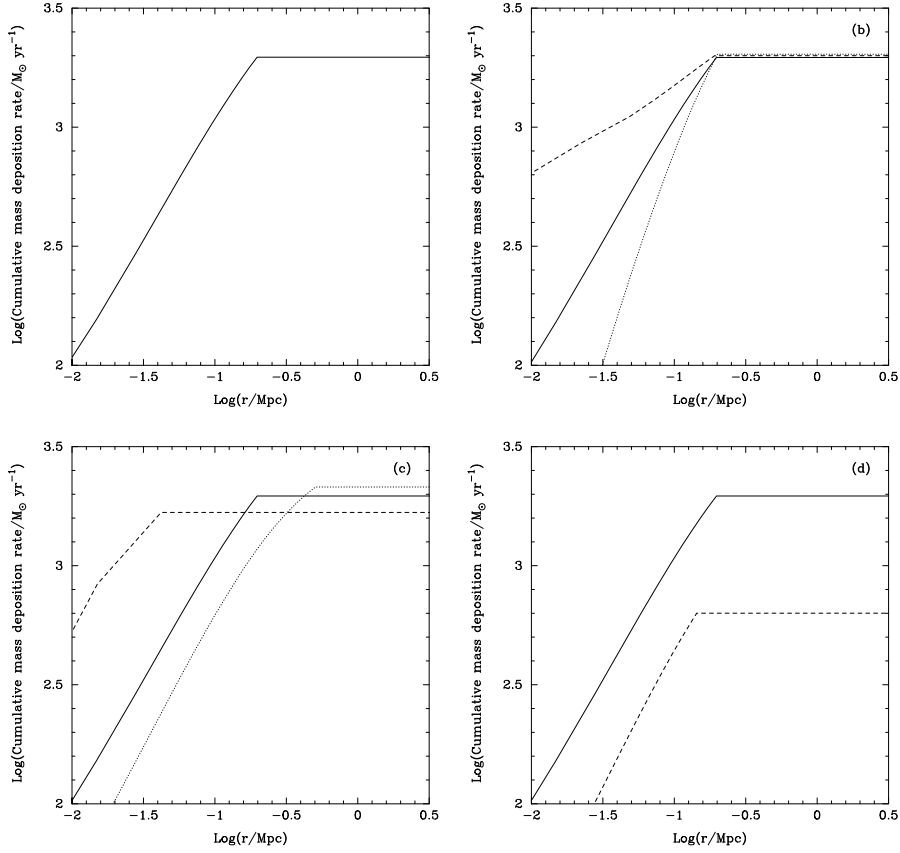


Figure 7: Final cumulative mass deposition rate for the $M_{vir} = 1.6 \times 10^{15} M_{\odot}$ model. Panels show (a) $\xi = 1.7$, $\alpha_{md} = 1.0$, $f_{gas} = 0.2$, (b) $\xi = 1.7$, 1.0 and 2.5 (solid, dashed and dotted lines), (c) $\alpha_{md} = 1.0$, 0.2 and 5.0 (solid, dashed and dotted lines), and (d) $f_{gas} = 0.2$ and 0.1 (solid and dashed lines respectively).

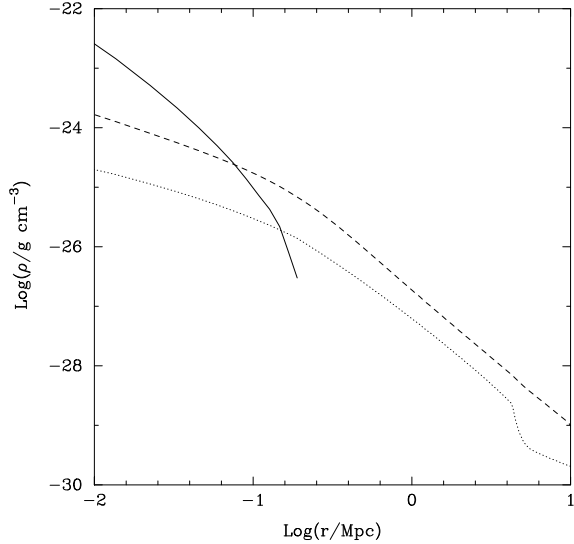


Figure 8: Final cooled gas, dark matter and gas density profiles for the $M_{vir} = 1.6 \times 10^{15} M_{\odot}$ model (solid, dashed and dotted lines respectively).

6.2 The Effects of Merging

Figure 9 shows the variation of total mass deposition rate with emission-weighted temperature for models of different mass. Two effects are apparent: (i) the mass deposition rates of the models are higher than those found observationally, and (ii) although the deposition rate increases with mass in the models, the trend is less steep than in observed clusters. For high mass systems, the models shown in Figure 9 appear to represent an upper bound to the observations, suggesting that some additional variable (perhaps cluster mergers) interrupts the idealised behaviour of the simulations. For example, if cooling flows are disrupted by major mergers and the time between such mergers is comparable to the timescale for the cooling flow to re-establish itself following a merger, then a wide range of mass deposition rates for clusters of a given richness might be expected.

In order to test this possibility, and also to explore the impact on our other results, we have performed a series of simulations in which the cooling flow is disrupted by raising the entropy of the gas within the cluster core ($r \leq 0.2R_{vir}$). The effect of this is to force gas out of the cluster core, temporarily reducing the mass deposition rate – Figure 10 shows the evolution of the mass deposition rate for a simulated rich cluster in which the cooling flow is disrupted several times during its evolution using this procedure. To determine whether cooling flow disruption can account for the scatter in the variation of mass deposition rate with cluster temperature, we have constructed some models in which the cooling flows are disrupted periodically, as would be expected in a Universe in which structures grow largely by hierarchical merging. We assume that clusters typically experience a major merger each time the Universe doubles its age (see e.g. Lacey & Cole 1993; Kauffmann & White 1993), but we also introduce some scatter in the merger times, such that the n th major merger occurs *on average* at time t^n , where $t^n = 2t^{n-1}$, with the *actual* merger time being chosen randomly from the range $(t^{n-1} + t^n)/2 \rightarrow (t^n + t^{n+1})/2$. The results from 80 such models are shown in Figure 11.

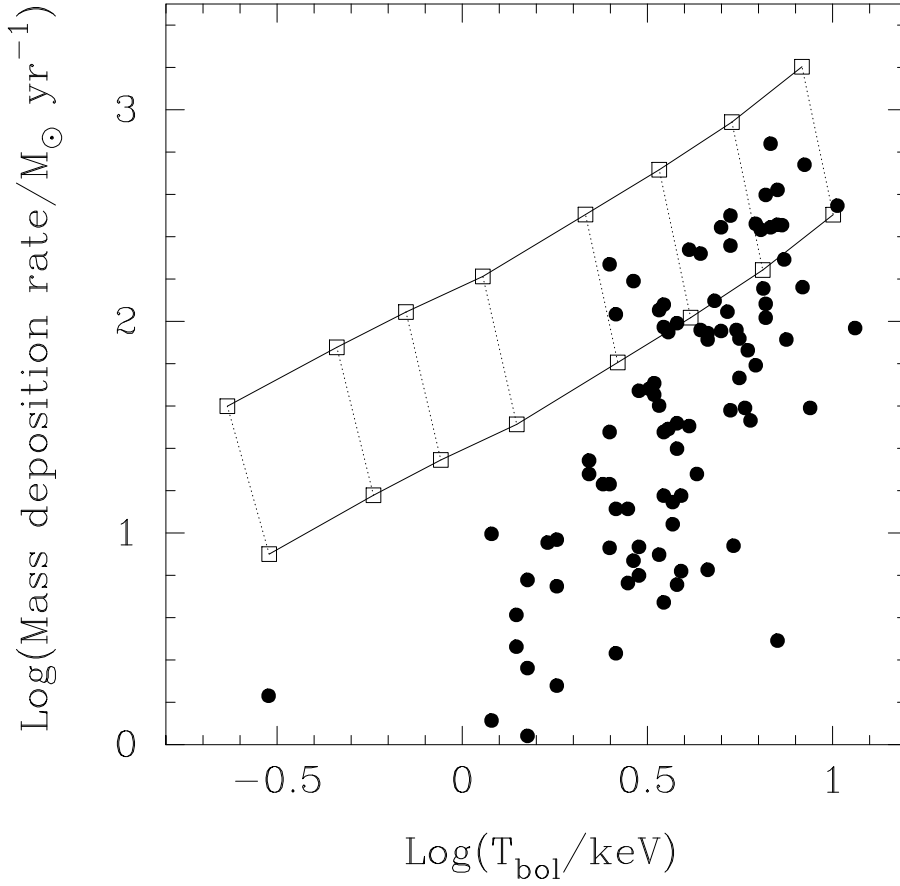


Figure 9: Final total mass deposition rate plotted against emission-weighted temperature for models of mass $M_{vir} = 7.8 \times 10^{12} M_{\odot}$, $2.0 \times 10^{13} M_{\odot}$, $3.9 \times 10^{13} M_{\odot}$, $7.8 \times 10^{13} M_{\odot}$, $2.0 \times 10^{14} M_{\odot}$, $3.9 \times 10^{14} M_{\odot}$, $7.8 \times 10^{14} M_{\odot}$ and $1.6 \times 10^{15} M_{\odot}$. The lower line shows the effect of scaling the mass deposition rate down by a factor of five. The observational data are taken from White, Jones & Forman (1996).

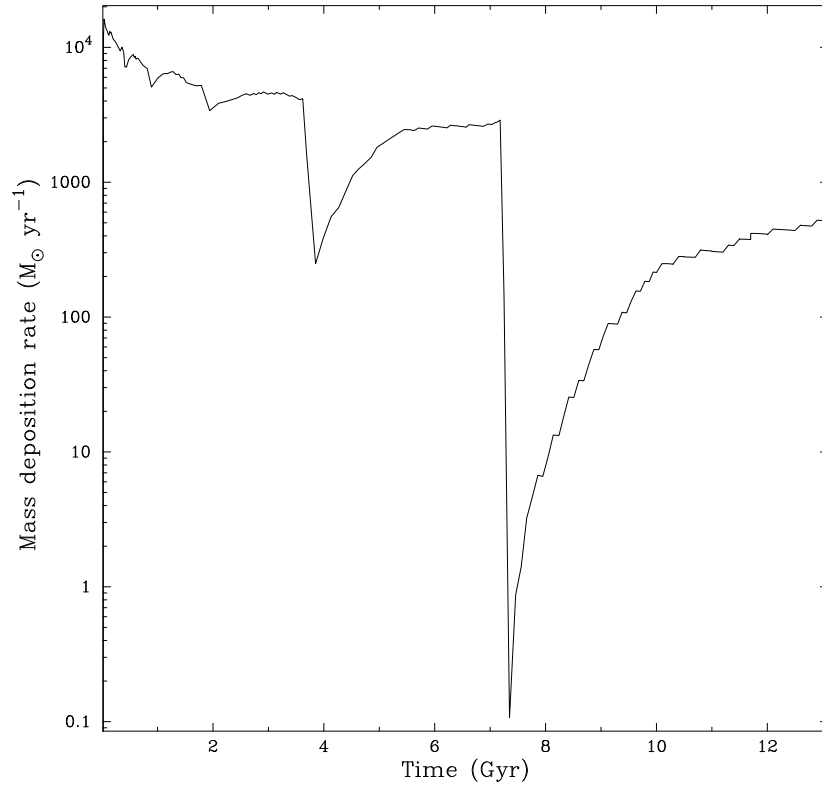


Figure 10: Evolution of the total mass deposition rate for a model of mass $M_{vir} = 1.6 \times 10^{15} M_{\odot}$ in which the cooling flow is disrupted using the procedure described in the text at several redshifts.

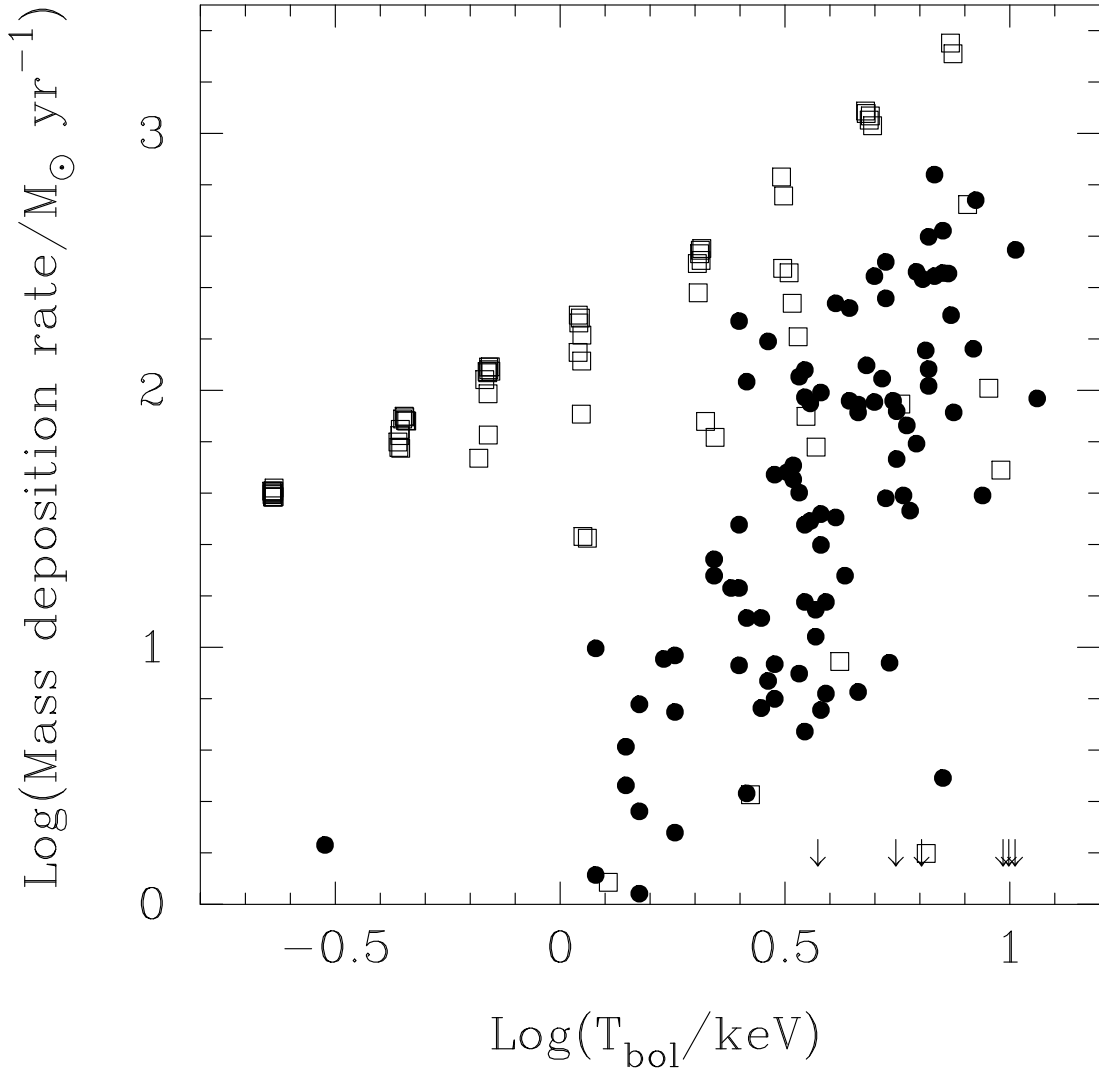


Figure 11: Final total mass deposition rate plotted against emission-weighted temperature for the cooling flow disruption models described in the text. The filled circles are observational data taken from White, Jones & Forman (1996), and the arrows indicate model clusters with $\dot{M} < 1 M_{\odot} \text{ yr}^{-1}$.

Cluster	Mean cluster temperature [†] \bar{T}/keV	Final virial mass of model M_{vir}/M_{\odot}	Final mean model temperature \bar{T}/keV
Hickson 62	0.96	7.8×10^{13}	1.1
A1060	2.55	2.0×10^{14}	2.2
MKW 3	3.0	3.9×10^{14}	3.4
A1795	5.34	7.8×10^{14}	5.4

[†] Ponman & Bertram 1993; Yamashita 1992

Table 2: Mean temperatures for the clusters in Figure 12a–d.

Clearly, disruption of the cooling flow can substantially reduce the present day mass deposition rates for the more massive systems since, for these systems, the timescale for the cooling flow to re-establish itself is comparable to the time between mergers. However, the low mass systems have substantially lower cooling times in their cores and the cooling flow is able to re-establish itself much faster, hence they are, on average, little affected by cooling flow disruption. For massive systems, the scatter in the mass deposition rate for a given temperature appears to be similar to that observed, but high resolution 3-D simulations with radiative cooling are needed to definitively establish the effects of cluster merging on cooling flows.

6.3 Evolution of the Cooling Flow

The evolution of the mass deposition rate is shown for a range of system masses in Figure 12. The mass deposition rate is substantially (a factor of 2–3) larger at $z = 5$ than at $z = 0$, decreasing with time due to the inflow of higher entropy gas from larger radii to replace that deposited at the cluster centre. This lowers the central gas density, which in turn reduces the mass deposition rate. As a result, most deposition occurs at high redshift, with $\sim 55\%$ of the total amount dropped by $z \simeq 1$.

7 THE GAS DISTRIBUTION

7.1 The X-ray Surface Brightness Profile

Final $z = 0$ bolometric surface brightness profiles for different mass models are shown in Figure 13, together with observed profiles for groups and clusters of comparable mass (Table 2). The observational profiles are based on *ROSAT* PSPC data converted to bolometric flux using *ROSAT* or *Ginga* temperatures, assuming isothermal gas (Cannon, Ponman & Navarro, in preparation). The model profiles were calculated by integrating the emission from the shells along each line of sight, using the cooling function of Raymond, Cox & Smith (1976). An additional component due to gas cooling to zero temperature at a rate proportional to the local mass deposition rate was also included.

The surface brightness profiles of the more massive systems are similar to, but slightly steeper than, those of observed clusters of similar mass: at the centre, the very large contribution of mass deposition to the cluster luminosity is clearly visible as a region of excess emission. Beyond this region, the surface brightness profile gradually steepens with radius. The shape of the *EVOL* surface brightness profiles of the richer systems are quite similar to the observed profiles outside the central region. However, unlike the *EVOL* profiles, there is no evidence for a region of greatly

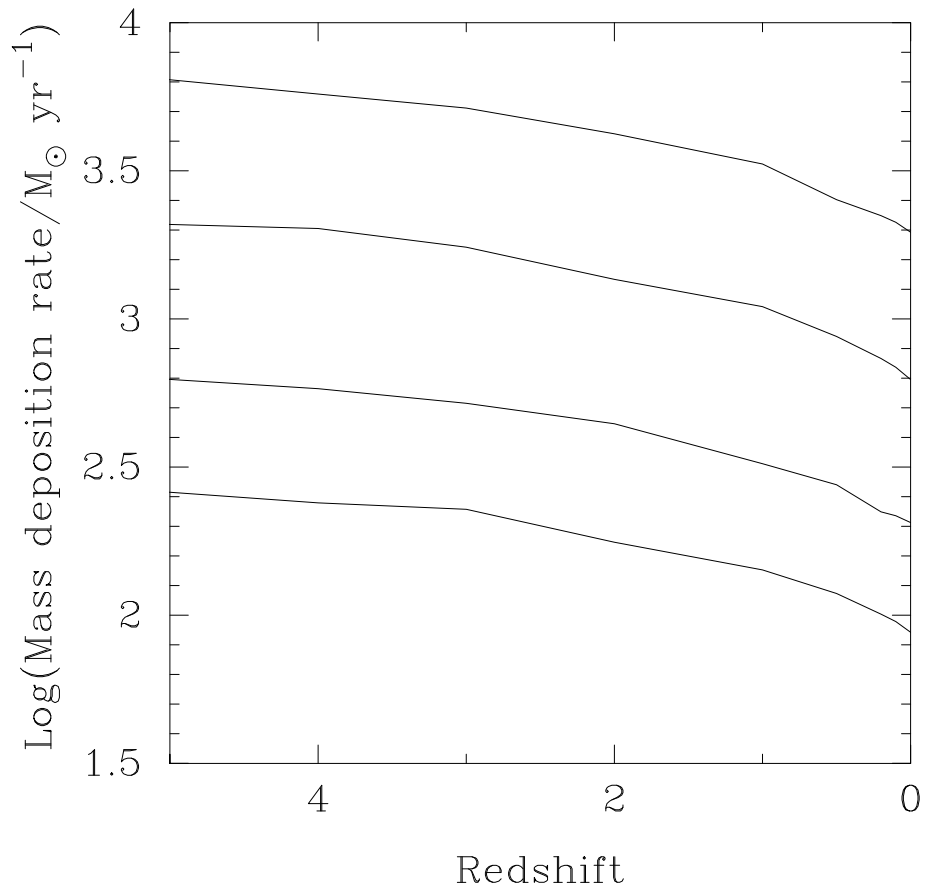


Figure 12: Evolution of the mass deposition rate for models with (from top to bottom) $M_{vir} = 1.6 \times 10^{15} M_{\odot}$, $3.9 \times 10^{14} M_{\odot}$, $7.8 \times 10^{13} M_{\odot}$, and $2.0 \times 10^{13} M_{\odot}$.

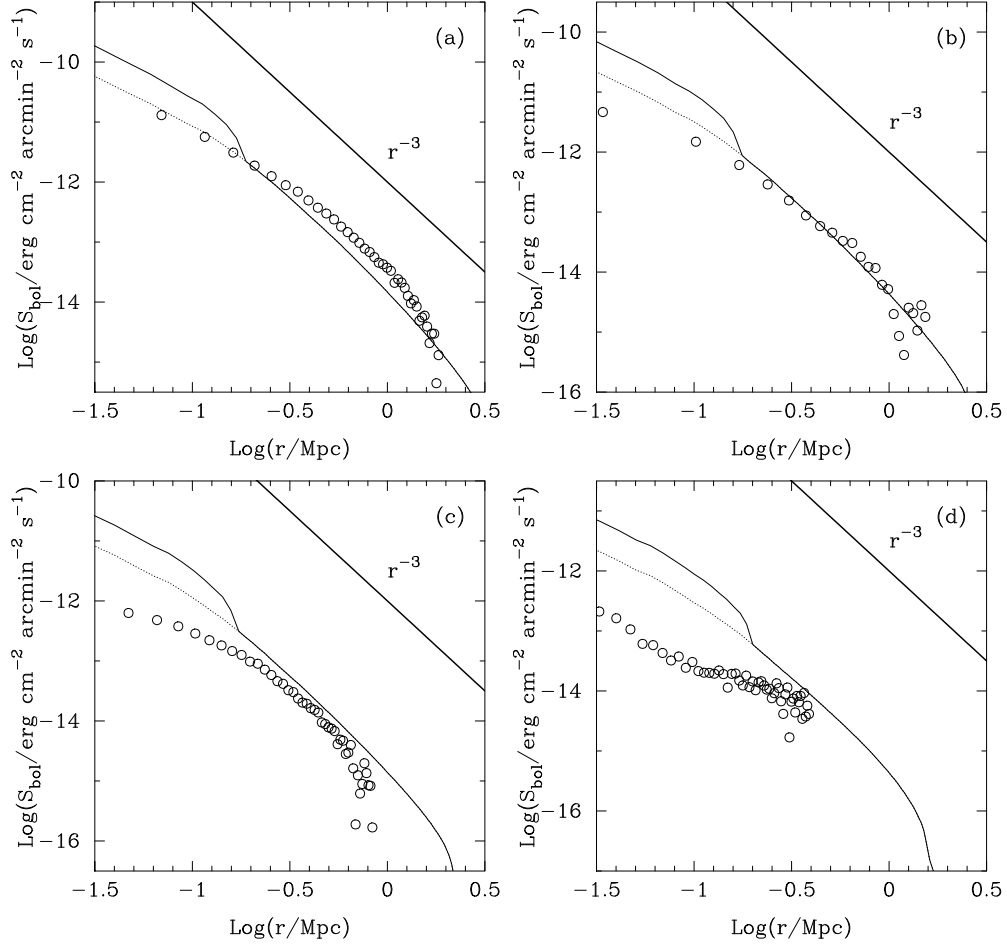


Figure 13: Final bolometric surface brightness profiles for systems of mass (a) $M_{vir} = 7.8 \times 10^{14} M_{\odot}$, (b) $M_{vir} = 3.9 \times 10^{14} M_{\odot}$, (c) $M_{vir} = 2.0 \times 10^{14} M_{\odot}$ and (d) $7.8 \times 10^{13} M_{\odot}$. The dotted line shows the surface brightness when the mass deposition luminosity is ignored. The circles indicate the surface brightness profiles of the following clusters observed by the *ROSAT* PSPC (D. Cannon, private communication; Ponman & Bertram 1993): (a) A1795, (b) MKW3, (c) A1060, and (d) Hickson 62. Note that the models have not been optimised to match the data, which are illustrative only. The relationship $S \propto r^{-3}$ is shown for reference, and $H_0 = 50 \text{ km s}^{-1} \text{ Mpc}^{-1}$ is assumed.

enhanced emission due to mass deposition within the cooling flow near the centre of observed clusters (though the isothermal assumption may in practice lead to an underestimate of the bolometric surface brightness by $\sim 20\%$ within the cooling flow region). The mismatch between the models and data near the centre persists even if the numerical parameters in *EVOL* are adjusted to confine the mass deposition to a region closer to the cluster centre. The discrepancy could be resolved if the cooling flows of real clusters are periodically disrupted (Section 6). As can be seen from the figure, the model profiles of the massive systems match the data much better if the emission from the model cooling flow is omitted.

A fit of the function

$$S(r) = S(0) \left[1 + \left(\frac{r}{r_c} \right)^2 \right]^{-3\beta_{fit}+1/2}, \quad (8)$$

to the underlying cluster emission (i.e., *excluding* the additional luminosity due to mass deposition) between $r = 0$ and $0.5R_{vir}$ yields a β_{fit} value of ~ 0.72 . This is slightly larger than inferred from observations of rich clusters, which generally yield $\langle \beta_{fit} \rangle \simeq 0.67$ and hence $S_x \propto r^{-3}$ outside the core (Jones & Forman 1984).

For lower mass clusters, the emission from the models falls above that found observationally, with the largest discrepancy being found in the smallest systems. This suggests that the gas fraction in the inner regions declines from rich clusters to groups, as found by David, Jones & Forman (1995).

7.2 β_{fit} vs Temperature and the Gas Entropy

Figure 14 shows the variation of β_{fit} with emission-weighted temperature at $z = 0$ for models of different mass. Also shown are values of β_{fit} from an observed sample (David, Jones & Forman 1995).

The results confirm those of Section 7.1 – there is a modest trend for a decrease in β_{fit} with decreasing \overline{T} , although β_{fit} is found to drop substantially for the lowest mass system, probably due to the importance of line cooling. Reasonable agreement with observations is found for the rich systems which have $\beta_{fit} \simeq 0.68$, very similar to the values found observationally ($\beta_{fit} \simeq 0.67$). There is, however, a large discrepancy between the simulated clusters and observations for the poorer clusters. Observationally, β_{fit} is found to decline steeply with decreasing T , which suggests the presence of an additional mechanism operating in poorer systems that has not been included in the simulations presented here.

Another pointer to the need for additional physical processes in low mass systems is the value of the entropy of the intracluster gas. Gas in the inner regions of X-ray bright galaxy groups (outside any cooling flow) is observed to have an entropy corresponding to $S = T/n^{2/3} \sim 200 - 300 \text{ keV cm}^2$ (Bourner and Ponman, paper in preparation) – very similar to that found in cluster cores. In the *EVOL* models presented here, the gas entropy at the corresponding point in rich systems has $S \sim 200 - 400 \text{ keV cm}^2$, as observed, but in the low mass models ($T \sim 1 \text{ keV}$) it has $S \lesssim 50 \text{ keV cm}^2$.

7.3 The Gas Mass Fraction Profile

Figure 15 shows the final enclosed gas mass fraction profiles for different mass models. In each case, the processes of cooling and mass deposition, particularly at early epochs, lead to the development of a profile that rises continually with radius (gas which has cooled out is counted as mass, but not as ‘gas’). Such a rise is similar to that inferred by White & Fabian (1995) from a sample of Abell clusters, and also agrees reasonably well with the results of David, Jones & Forman (1995). The mechanism behind this is interesting – since the entropy of the gas increases with radius, mass deposition near the cluster centre leads to the inflow of higher entropy gas from further out in

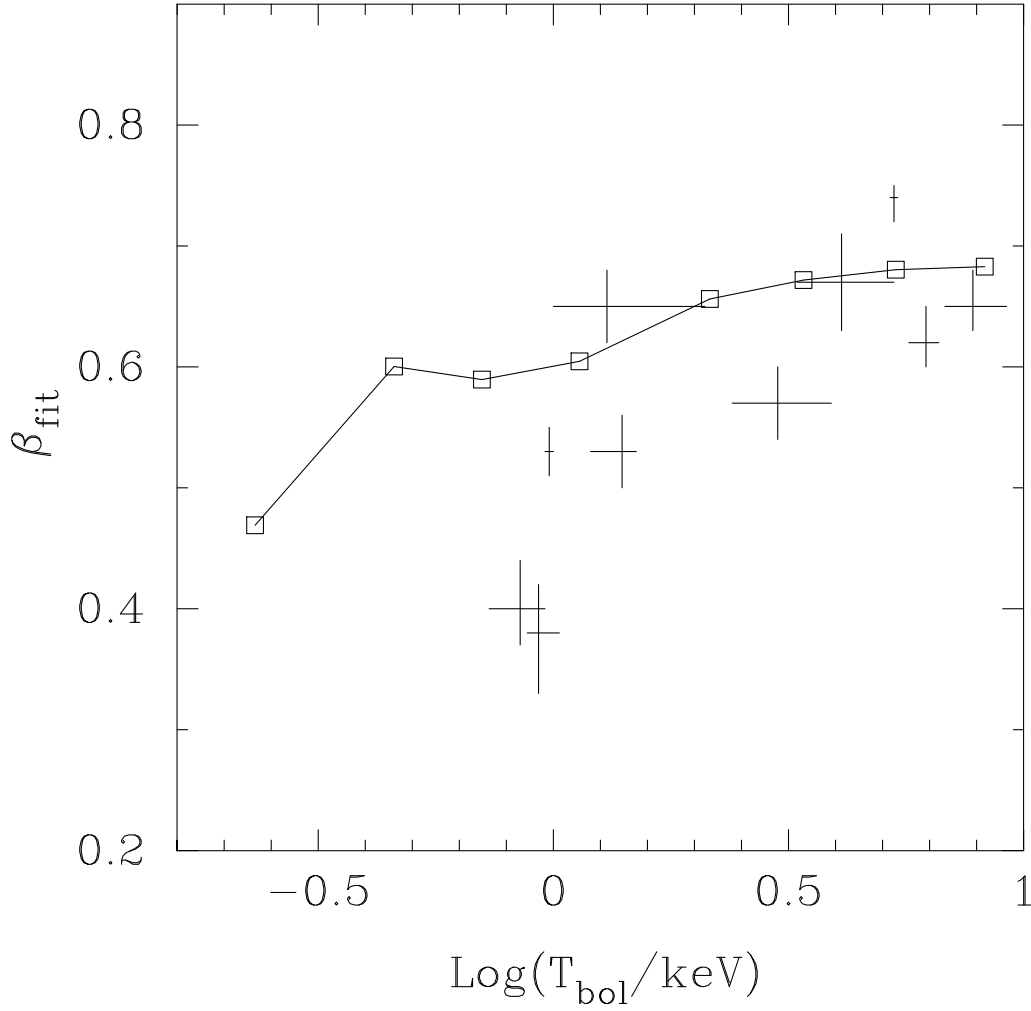


Figure 14: Final β_{fit} plotted against emission-weighted temperature for models of mass $M_{vir} = 2.0 \times 10^{13} M_{\odot}$, $3.9 \times 10^{13} M_{\odot}$, $7.8 \times 10^{13} M_{\odot}$, $2.0 \times 10^{14} M_{\odot}$, $3.9 \times 10^{14} M_{\odot}$, $7.8 \times 10^{14} M_{\odot}$ and $1.6 \times 10^{15} M_{\odot}$. The observational data (crosses) are taken from David, Jones & Forman (1995).

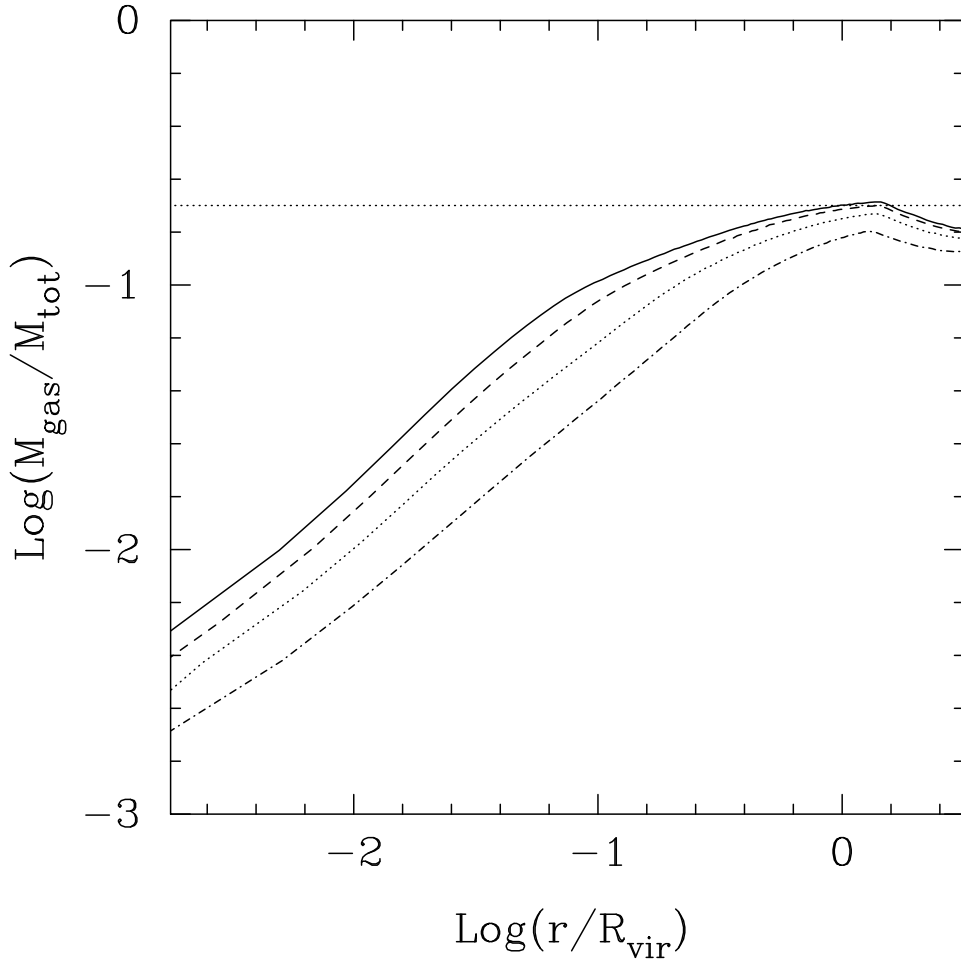


Figure 15: Final enclosed gas mass fraction profiles for models of mass $M_{\text{vir}} = 1.6 \times 10^{15} M_{\odot}$, $3.9 \times 10^{14} M_{\odot}$, $7.8 \times 10^{13} M_{\odot}$ and $2.0 \times 10^{13} M_{\odot}$ (solid, dashed, dotted, dot-dash lines respectively). The horizontal dotted line shows the global value.

the cluster which, in turn, lowers the central gas density producing a gas “core”. The *total* mass density profile is, however, quite sharply peaked despite the core in the dark matter profile, being dominated by “cooled” gas at small radii (Figure 8). The net result is a gas mass fraction profile that increases with radius. The slight decline in f_{gas} seen outside R_{vir} arises from the fact that the gas density drops sharply at an outward propagating shock, whilst the dark matter density (which is represented by a cored power law model, as discussed in section 2.3) declines smoothly to the background value.

Although central cooling and consequent gas inflow does produce a rising gas fraction profile, in accord with observations, it involves mass deposition rates, particularly at large redshift, which are much larger than those typically inferred for nearby clusters. Alternatively, there are several possible mechanisms, such as major mergers, and energy injection from the cluster galaxies, which may be effective at forcing gas out of the cluster core – this would reduce the gas fraction in the inner regions, and should also lower the mass deposition rate in the cooling flow.

Figure 15 also shows that f_{gas} in the inner regions declines somewhat with decreasing system size, due to the greater importance of cooling in lower mass systems.

7.4 The Effect of a Fully Multiphase ICM

Since the cooling time threshold for the onset of multiphase mass deposition is somewhat arbitrary, we have examined the alternative possibility that the bulk of the ICM is multiphase by constructing some models in which mass deposition is allowed to occur throughout the cluster ($\alpha_{md} = \infty$). The final ($z = 0$) surface brightness profile for such a model of mass $M_{vir} = 7.8 \times 10^{14} M_{\odot}$ is shown in Figure 16. The shape of the surface brightness profile is similar to that of observed clusters, but the contribution of the cooling gas to the cluster luminosity is appreciable at all radii ($\sim 70\%$ of the total luminosity). This reduces the gas fraction required for a given cluster luminosity by $\sim 70\%$ and would be a possible mechanism for alleviating the “baryon catastrophe” associated with clusters of galaxies (Gunn & Thomas 1995). However, it was shown some time ago by Allen *et al.* (1992) that the spectral properties of the intracluster emission in the Perseus cluster are inconsistent with such large scale multiphase structure, and this conclusion has been confirmed for other systems by ASCA (Mushotzky *et al.* 1996).

8 X-RAY LUMINOSITY

8.1 Luminosity-Temperature Relation

Figure 17 shows the bolometric luminosity, L_{bol} , plotted against emission-weighted temperature, T_{bol} , for various models. The calculation of T_{bol} includes the contribution of mass deposition within the cooling flow. For the hottest models, this “cooling luminosity” lowers the emission-weighted temperature by up to $\sim 30\%$. If the structure of all clusters is self-similar then scaling relations can be derived for the evolution of mean cluster properties. One of the predictions of self-similarity is a relationship between bolometric luminosity and temperature of the form $L_{bol} \propto T^2$ (NFW96), much flatter than the observed relationship, $L_{bol} \propto T^{2.81 \pm 0.18}$ (White, Jones & Forman 1996).

The slope of the $L : T$ relation for the infall models considered here is 2.1 (2.2 if the mass deposition rate is reduced by a factor of five), which is still flatter than that found observationally. In order to investigate the effects of cooling on the lower mass systems, some simulations were performed in which radiative cooling was turned off during the cluster evolution. The results of viewing the X-ray emission from such a model at $z = 0$ are shown in Figure 18. (The surface brightness profiles of these models are so steep that the luminosity diverges at small radii so, for these models only, emission within a radius of $0.05R_{vir}$ has been ignored.) The greater importance of line cooling to the bolometric luminosity for the low mass systems causes the $L : T$ relation to

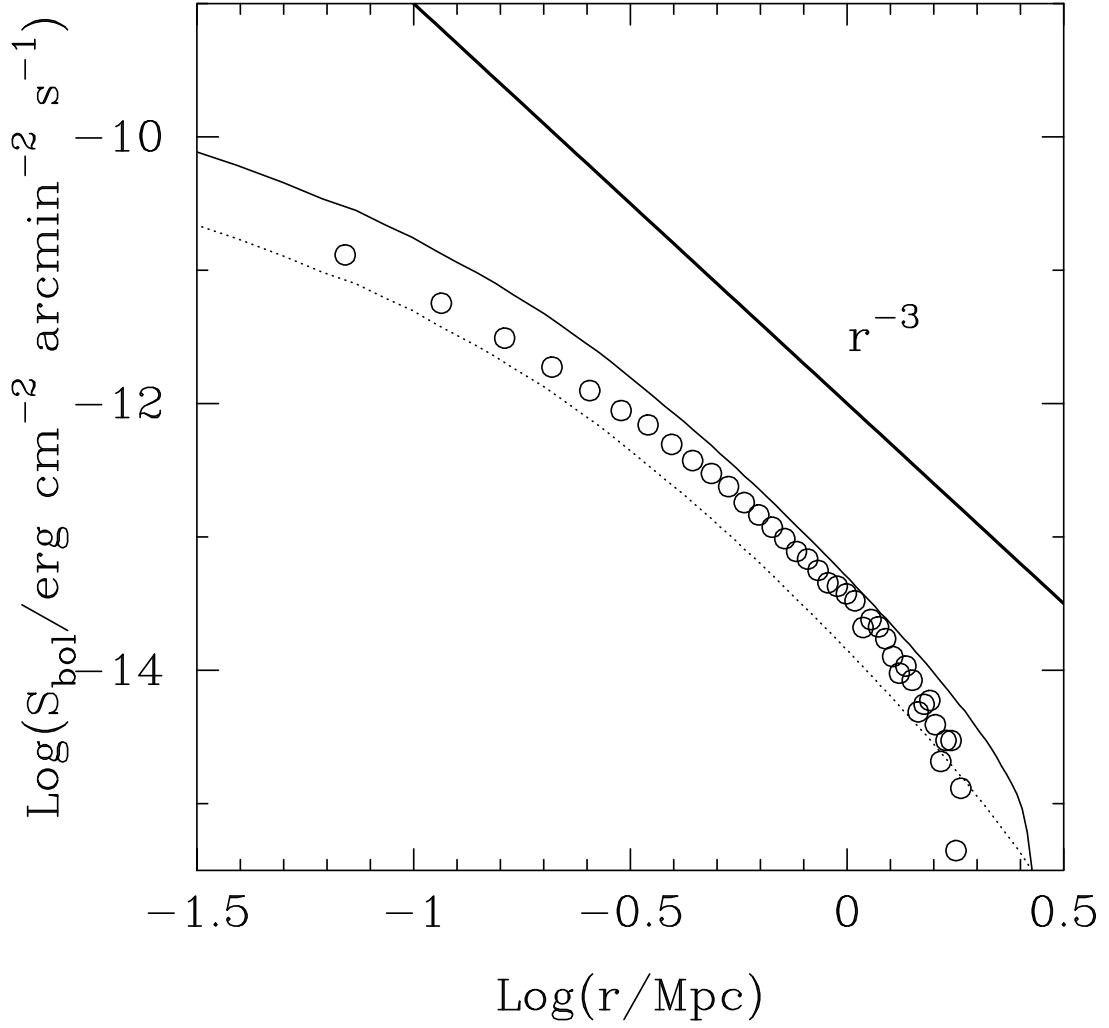


Figure 16: Final bolometric surface brightness profiles for a fully multiphase ICM model of mass $7.8 \times 10^{14} M_{\odot}$. The dotted line shows the surface brightness when the mass deposition luminosity is ignored. The circles indicate the surface brightness profile of A1795 observed by the *ROSAT* PSPC (D. Cannon, private communication).

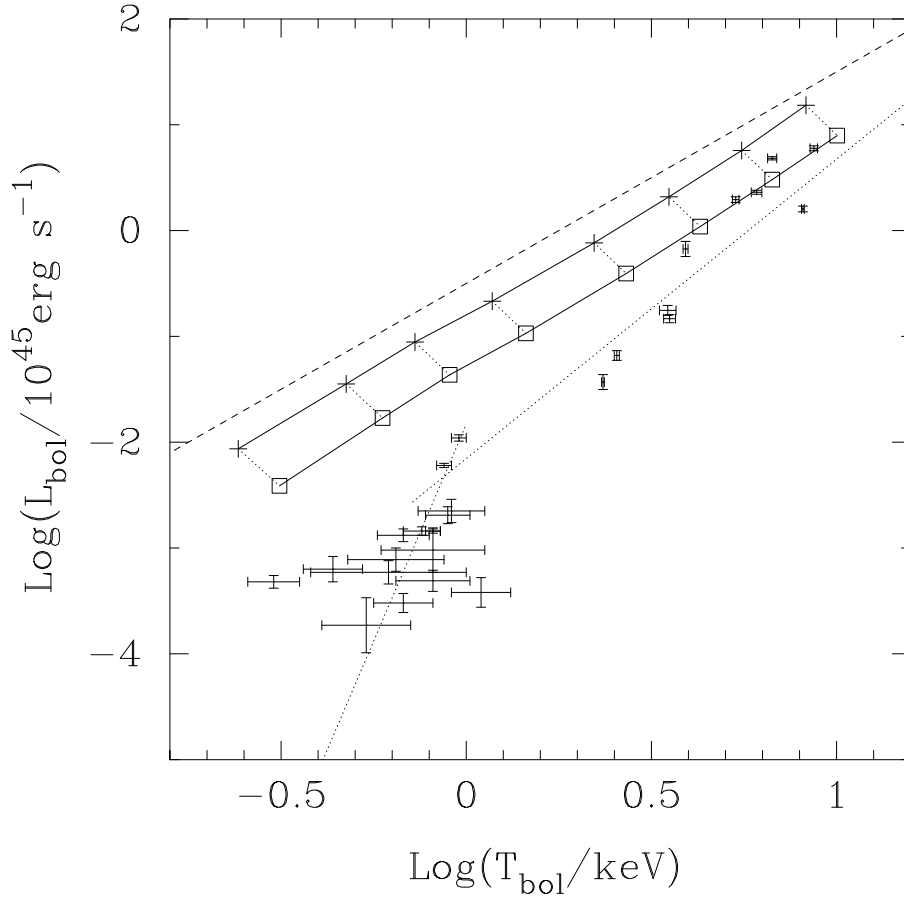


Figure 17: Bolometric luminosity plotted against temperature for models of mass $M_{\text{vir}} = 7.8 \times 10^{12} M_{\odot}$, $2.0 \times 10^{13} M_{\odot}$, $3.9 \times 10^{14} M_{\odot}$, $7.8 \times 10^{13} M_{\odot}$, $2.0 \times 10^{14} M_{\odot}$, $3.9 \times 10^{14} M_{\odot}$, $7.8 \times 10^{14} M_{\odot}$ and $1.6 \times 10^{15} M_{\odot}$. The lower line shows the effect of scaling the mass deposition rate down by a factor of 5. The data points are from Ponman *et al.* (1996), and the dashed line (which has arbitrary normalisation) shows the relation, $L \propto T^2$, expected for self-similar cluster structure.

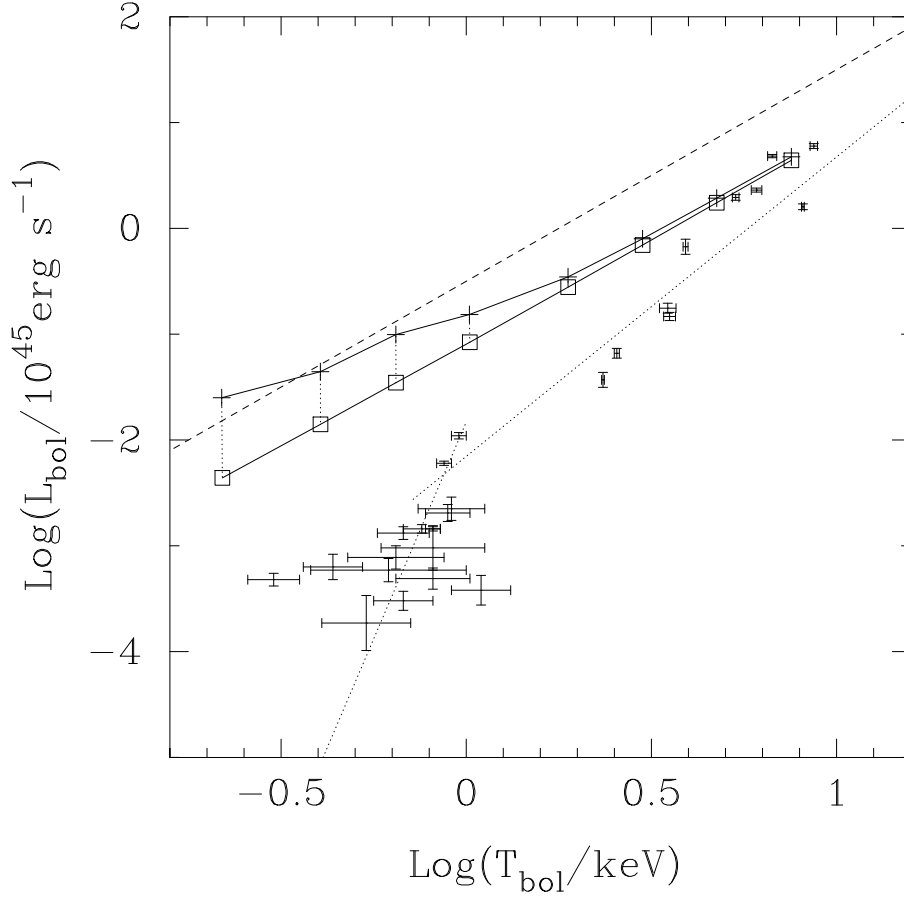


Figure 18: Bolometric luminosity plotted against temperature for models in which radiative cooling has been turned off during the evolution. The masses of the clusters are $M_{\text{vir}} = 7.8 \times 10^{12} M_{\odot}$, $2.0 \times 10^{13} M_{\odot}$, $3.9 \times 10^{14} M_{\odot}$, $7.8 \times 10^{13} M_{\odot}$, $2.0 \times 10^{14} M_{\odot}$, $3.9 \times 10^{14} M_{\odot}$, $7.8 \times 10^{14} M_{\odot}$ and $1.6 \times 10^{15} M_{\odot}$. The lower line shows the effect of setting the metal abundance to zero when calculating the luminosity and mean temperature. The data points are from Ponman *et al.* (1996), and the dashed line (which has arbitrary normalisation) is the prediction for self-similar cluster structure, $L \propto T^2$.

flatten at low temperatures. However, when line radiation is neglected, the logarithmic slope of the $L : T$ relation is 1.95, very close to the value of 2 expected if the cluster population is self-similar, with different mass clusters having profiles of the same form.

This test shows that the fact that the slope of the $L : T$ relation in Figure 17 is so similar to that expected for self-similar scaling is somewhat fortuitous. It occurs because the flattening in the relation due to the increased contribution of line emission and mass deposition in low mass systems is compensated by the fact that this extra mass deposition lowers the gas fraction, which steepens the $L : T$ relation. The net result is an $L : T$ index only slightly steeper than 2.

The second effect which is apparent in Figure 17 is that the normalisation of the luminosity of the simulated clusters is larger than that observed. This discrepancy is partly due to the fact that the mass deposition rates are considerably larger than typically inferred from observations. The contribution of this cooling material to the overall cluster luminosity is significant (see Figure 13) – this is a generic feature of the simple infall models, possibly compounded by the simplified radial cooling flow.

In Figure 19 we show the $L : T$ relation for the set of merger models discussed in Section 6.2. The effects of merging are to substantially reduce the luminosity of the more massive ($T \gtrsim 3$ keV) systems, bringing them into line with observed clusters. However, as noted in Section 6.2, the effect of merging on lower mass systems is much less marked, due to the speed with which the system recovers from a merger, and re-establishes its cooling flow.

8.2 Luminosity Evolution

The evolution of the bolometric luminosity for models with a range of masses is shown in Figure 20. X-ray emission is generally detectable out to 0.2–0.5 Mpc and ~ 2 Mpc for groups and clusters respectively (Mulchaey *et al.* 1996; Ponman *et al.* 1996; White & Fabian 1995), corresponding to a radius of $\sim 0.5R_{vir}$. Accordingly, the luminosities given here were calculated by summing the emission from shells within a radius of $0.5R_{vir}$. A line showing the evolution expected if the gas distribution is self-similar (e.g., if $\rho_{gas}(r) \propto \rho_{dark}(r)$) is also shown in Figure 20,

$$L_{bol} \propto (1+z)^{(13+7n)/(6+2n)}. \quad (9)$$

This relation is found to give a very good match to the evolution of the models with no radiative cooling. However, as shown in the figure, models with radiative cooling evolve much less strongly – the cluster luminosity rises by $\sim 50\%$ out to $z = 0.5$, while Equation 9 gives a rise of $\sim 80\%$ for $n = -1$ over the same interval. The difference is predominantly due to evolution of the central gas mass fraction: at earlier epochs, the characteristic density of the virialised region is higher and mass deposition more widespread, resulting in a lower gas mass fraction within any fixed fraction of the virial radius (see Figure 5). As a result, the gas mass fraction rises with time compared to the self-similar scaling, reducing the evolution of the luminosity. Such modest ($\sim 30\%$ out to $z = 0.3$) positive evolution of the X-ray luminosity of rich clusters is consistent with recent results from clusters observed during the *ROSAT* All Sky Survey (H. Ebeling, private communication).

9 THE EFFECT OF $\Omega_0 < 1$

In order to test the extent to which the results are sensitive to the assumed value of Ω_0 , a few models have been considered in which $\Omega_0 < 1$. In this case, the evolution of the dark matter density departs significantly from the self-similar behaviour at redshifts $z \lesssim z_{crit} = \Omega_0^{-1} - 1$ (Lacey & Cole 1993). To simulate the approximate evolution of a cluster in an open Universe, it is assumed that the dark matter density behaves exactly as in the $\Omega = 1$ case for $z > z_{crit}$, whilst for $z < z_{crit}$ the dark matter density beyond a radius of $r_{crit} = 5R_{vir}$ (roughly the radius at which material is

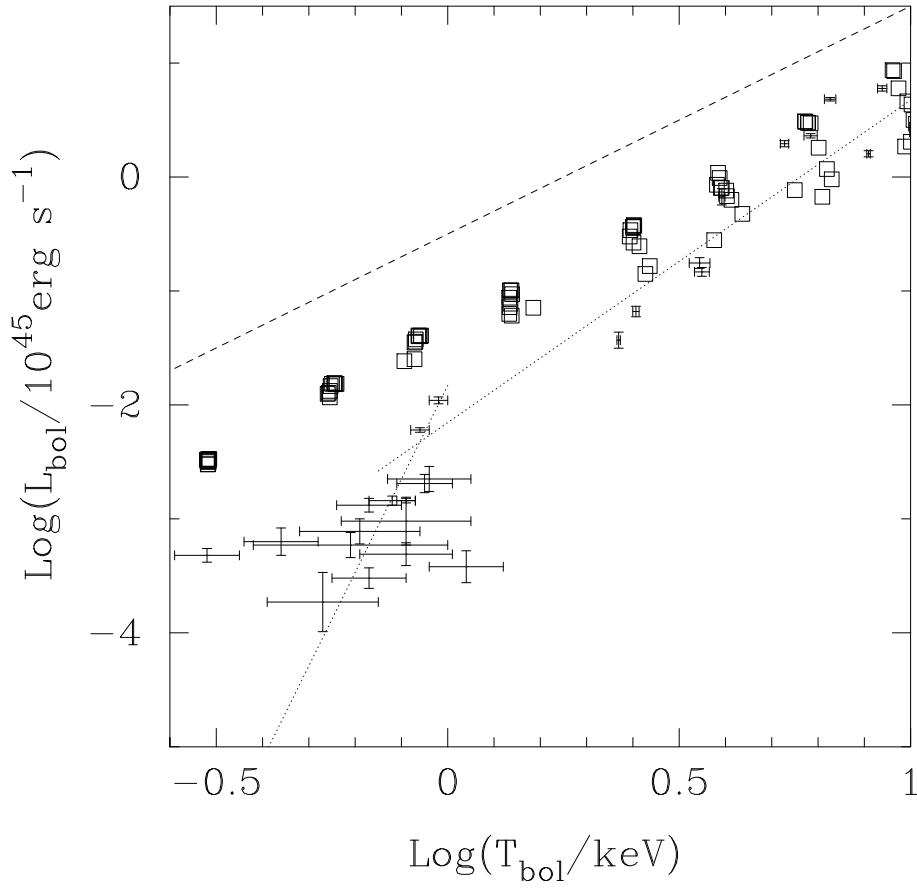


Figure 19: Final bolometric luminosity plotted against emission-weighted temperature for cooling flow disruption models. The data points are from Ponman *et al.* (1996), and the dashed line (which has arbitrary normalisation) shows the relation, $L \propto T^2$, expected for self-similar cluster structure.

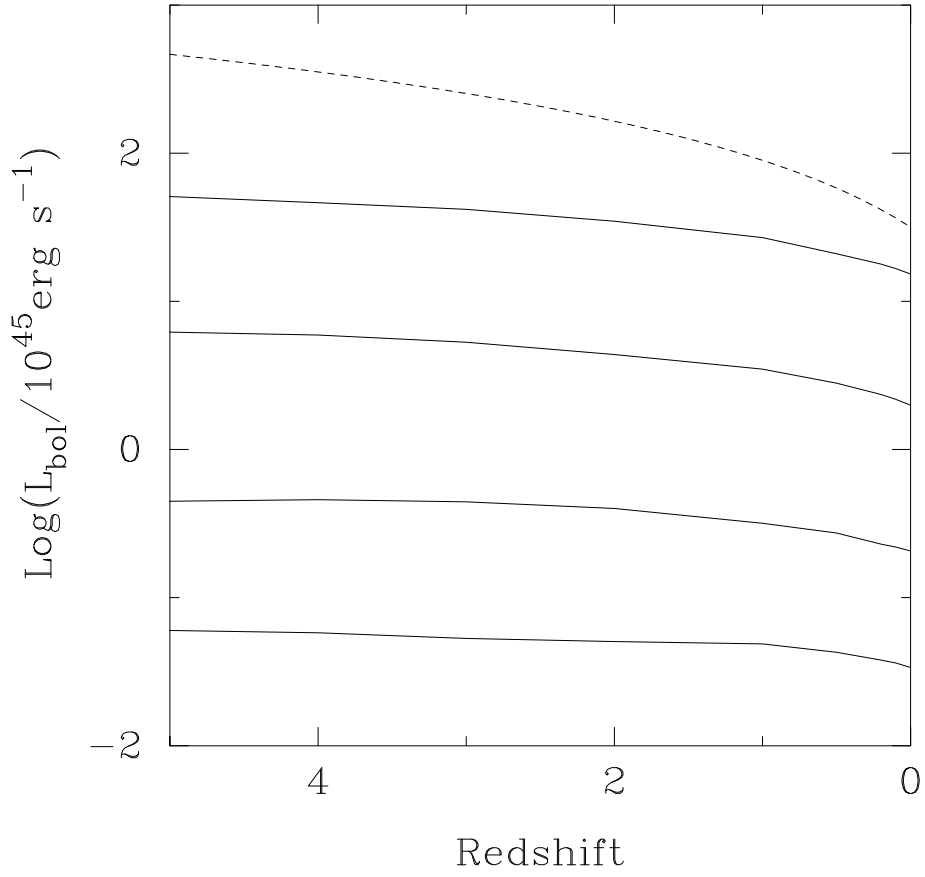


Figure 20: Evolution of the bolometric luminosity for models of mass (from top to bottom) $M_{\text{vir}} = 1.6 \times 10^{15} M_{\odot}$, $3.9 \times 10^{14} M_{\odot}$, $7.8 \times 10^{13} M_{\odot}$, and $2.0 \times 10^{13} M_{\odot}$. The dashed line shows the self-similar prediction.

just turning around from the Hubble expansion) is constant, and equal to the mean density of the universe at that epoch.

The treatment of the dark matter within r_{crit} after $z = z_{crit}$ is somewhat problematic, due to uncertainty in the evolution of the dark matter “core”. We consider two cases: (1) at $z = z_{crit}$, the profile within r_{crit} is frozen and there is no subsequent evolution, and (2) the dark matter profile within r_{crit} is allowed to evolve in the same way as in the critical density case. Clearly the behaviour of the low Ω_0 models in both cases will be unrealistic at large radius – the density at r_{crit} will suddenly drop into the background, whereas in reality one would expect a gradual steepening of the density profile at large radius (Hoffman & Shaham 1985; Crone, Evrard & Richstone 1994). However, the dynamics in the central region, which contributes most of the luminosity, will be relatively unaffected by this.

Figure 21 compares the evolution of the luminosity for two $\Omega_0 = 0.3$ models (which differ in the handling of the core evolution as discussed above) and an $\Omega_0 = 1$ model, all with $M_{vir} \approx 1.0 \times 10^{15} M_\odot$ at $z = 0$, and a gas fraction of 0.3. Clearly the dependence of the luminosity evolution on Ω_0 , and on the treatment of the core in the $\Omega_0 = 0.3$ models, is slight. The weakness of the dependence on Ω_0 comes about because the luminosity is dominated by gas in the central regions, which has a very similar profile in the $\Omega_0 = 0.3$ and $\Omega_0 = 1$ cases. Significant differences occur at large radii, but these regions contribute little to the X-ray flux.

10 CONCLUSIONS

The 1-D simulations presented above, including an evolving potential and the effects of radiative cooling and distributed mass deposition, are reasonably successful at reproducing many of the observed properties of galaxy clusters. Temperature and density profiles are broadly realistic, and the inflow of higher entropy gas into the cluster core as a result of radiative cooling, leads to a gas fraction which rises with radius, in accord with observations. It also results in X-ray luminosity evolution which is milder than the self-similar prediction. The strong positive evolution of the latter is known to conflict with observation (Castander *et al.* 1994).

There are, however, some significant discrepancies with observation. The cooling flows produced by *EVOL* simulations are much stronger than those typically observed. This result is robust to changes in the values of numerical parameters in the simulations. The effects of subcluster merging, which are believed to periodically disrupt cooling flows, and are of course absent from a 1-D code, are likely to account for the lower cooling rates (and the substantial scatter for clusters of a given X-ray luminosity) seen in massive clusters. However in lower mass systems, the cooling flow re-establishes itself very quickly after disruption.

A number of further disagreements with observation for low mass systems suggest the need for additional physics in the models. The simulations reported here do give somewhat flatter surface brightness profiles (low β values – Figure 14) and lower gas fractions (Figure 15) in low mass systems, but the effects are much weaker than those observed. Also the slope of the $L : T$ relation does not steepen below $T \sim 1$ keV in the way which is observed (Figure 17). Perhaps most suggestive of all, is the observation that the simple models described in this paper underpredict the entropy of the gas in groups and poor clusters.

These differences suggest that some additional effects, which are most significant in low mass systems, have increased the entropy and reduced the density of gas in the inner regions of low mass systems. Possible mechanisms include heating of the gas to a temperature $\gtrsim 10^7$ K, either as the result of an early preheating era (Couchman & Rees 1986; Meiksin & Madau 1993) or the injection of galaxy winds (White 1991; Metzler & Evrard 1994), or increased efficiency of star formation in groups (David, Jones & Forman 1995).

The role of these additional mechanisms is explored in Paper II.

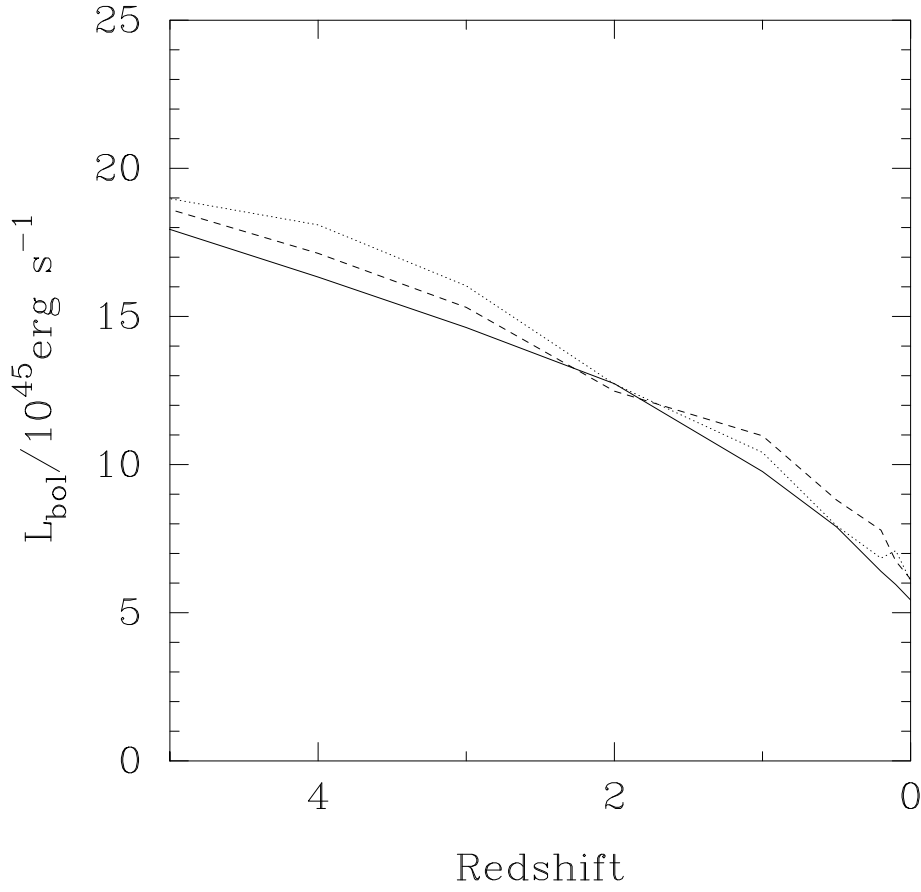


Figure 21: Evolution of the bolometric luminosity for models with (1) $\Omega_0 = 1$ and $M_{vir} = 1.6 \times 10^{15} M_\odot$ (solid line), (2) $\Omega_0 = 0.3$, $M_{vir} = 8.6 \times 10^{14} M_\odot$, and dark matter profile within R_{vir} frozen for $z > z_{crit}$ (dashed line), and (3) $\Omega_0 = 0.3$, $M_{vir} = 1.3 \times 10^{15} M_\odot$, and dark matter profile within R_{vir} allowed to evolve as in the $\Omega_0 = 1$ case (dotted line).

ACKNOWLEDGEMENTS

We would like to thank Peter Thomas and Richard Bower for help and discussions whilst this work was in progress, David White for a prepublication copy of his compilation of cluster properties, and Damian Cannon for the observed surface brightness profiles used in Section 7. Discussions with the referee, David Weinberg, resulted in improvements to the paper and to our understanding of self-similarity. The computations were carried out using the facilities of the Starlink node at the University of Birmingham. PAK acknowledges the support of the PPARC.

REFERENCES

- Allen S.W., Fabian A.C., Johnstone R.M., Nulsen P.E.J., Edge A.C., 1992, *MNRAS*, 254, 51
- Allen S.W., Fabian A.C., Kneib J.P., 1996, *MNRAS*, 279, 615
- Bertschinger E., 1985, *ApJ*, 58, 39
- Carr B., 1994, *ARA&A*, 32, 531
- Castander F.J., Ellis R.S., Frenk C.S., Dressler A., Gunn J.E., 1994, *ApJ*, 424, L79
- Couchman H.M.P., Rees M.J., 1986, *MNRAS*, 221, 53
- Crone M.M., Evrard A.E., Richstone D.O., 1994, *ApJ*, 434, 402
- David L.P., Forman W., Jones C., 1990, *ApJ*, 359, 29
- David L.P., Jones C., Forman W., 1995, *ApJ*, 445, 578
- Efstathiou G., Eastwood J.W., 1981, *MNRAS*, 194, 503
- Evrard A.E., 1988, *MNRAS*, 235, 911
- Evrard A.E., 1990, *ApJ*, 363, 349
- Eyles C.J., Watt M.P., Bertram D., Church M.J., Ponman T.J., Skinner G.K., Willmore A.P., 1991, *ApJ*, 376, 23
- Fabian A.C., Nulsen P.E.J., Canizares C.R., 1991, *Astronomy and Astrophysics Review*, 2, 191
- Fillmore J.A., Goldreich P., 1984, *ApJ*, 281, 1 (FG84)
- Gingold R.A., Monaghan J.J., 1977, *MNRAS*, 181, 375
- Gull S.F., Northover K.J.E., 1975, *MNRAS*, 173, 585
- Gunn K.F., Thomas P.A., 1996, *MNRAS*, submitted
- Hirayama Y., 1978, *Prog. Theor. Phys.*, 60, 724

Hoffman Y., Shaham J., 1985, *ApJ*, 297, 16

Hughes J.P., Gorenstein P., Fabricant D., 1988, *ApJ*, 329, 82

Jones C., Forman W., 1984, *ApJ*, 276, 38

Kaiser N., 1986, *MNRAS*, 222, 323

Katz N., White S.D.M., 1993, *ApJ*, 412, 455

Kauffmann G., White S.D.M., 1993, *MNRAS*, 261, 921

Knight P.A., 1996, Ph.D. thesis, University of Birmingham, UK

Lacey C., Cole S., 1993, *MNRAS*, 262, 627

Lea S.M., 1976, *ApJ*, 203, 569

Loewenstein M., Mushotzky R.F., 1996, *ApJ*, submitted

Markevitch M., 1996, *ApJ*, 465, L1

Markevitch M., Vikhlinin A., 1996, *ApJ*, submitted

Mathews W.G., Baker J.C., 1971, *ApJ*, 170, 241

Meiksin A., Madau P., 1993, *ApJ*, 412, 34

Metzler C.A., Evrard A.E., 1994, *ApJ*, 437, 564

Mulchaey J.S., Davis D.S., Mushotzky R.F., Burnstein D., 1996, *ApJ*, 456, 80

Mushotzky R., Loewenstein M., Arnaud K.A., Tamura T., Fukazawa Y., Matsushita K., Kikuchi K., Hatsukade I., 1996, *ApJ*, 466, 686

Navarro J.F., Frenk C.S., White S.D.M., 1996, *MNRAS*, 275, 720

Navarro J.F., Frenk C.S., White S.D.M., 1996, *ApJ*, 462, 563 (NFW96)

Oegerle W.R., Hoessel J.G., 1991, *ApJ*, 375, 15

Ostriker J.P., Gnedin N.Y., 1996, *ApJ*, submitted

Perrenod S.C., 1978, *ApJ*, 224, 285

Ponman T.J., Bertram D., 1993, *Nat*, 363, 51

Ponman T.J., Bourner P.D.J., Ebeling H., Böhringer H., 1996, *MNRAS*, in press

Raymond J.C., Cox D.P., Smith B.W., 1976, *ApJ*, 204, 290

Richtmyer R.D., Morton K.W., 1967, *Difference Methods for Initial Value Problems* (2d ed.; New

York: Interscience)

- Sarazin C.L., 1990, in *The Interstellar Medium in Galaxies*, ed H.A. Thronson Jr, J.M. Shull, Kluwer Academic
- Schindler S., Hattori M., Neumann D.M., Böhringer H., 1996, A&A, submitted
- Takahara F., Ikeuchi S., Shibazaki N., Hōshi R., 1976, Prog. Theor. Phys., 56, 1093
- Thomas P.A., 1988, MNRAS, 235, 315
- Thomas P.A., Couchman H.M.P., 1992, MNRAS, 257, 11
- Thoul A.A., Weinberg D.H., 1995, ApJ, 442, 480
- Tormen G., Bouchet F.R., White S.D.M., 1996, MNRAS, submitted
- Walker T.P., Steigman G., Kang H., Schramm D.M., Olive K.A., 1991, ApJ, 376, 51
- Watt M.P., Ponman T.J., Bertram D., Eyles C.J., Skinner G.K., Willmore A.P., 1992, MNRAS, 258, 738
- Waxman E., Miralda-Escudé J., 1995, ApJ, 451, 451
- White D.A., Fabian A.C., 1995, MNRAS, 273, 72
- White D.A., Jones C., Forman W.R., 1996, MNRAS, submitted
- White R.E., Sarazin C.L., 1987, ApJ, 318, 612
- White R.E., 1991, ApJ, 367, 69
- White S.D.M., 1976, MNRAS, 174, 19
- White S.D.M., Navarro J.N., Evrard A.E., Frenk C.S., 1993, Nat, 366, 429
- Yamashita K., 1992, in Tanaka Y., Koyama K. eds., *Frontiers of X-ray Astronomy*. Universal Academy Press, Tokyo. p.475